Ozone and carbon monoxide observations over open oceans on R/V *Mirai* from 67° S to 75° N during 2012 to 2017: Testing global chemical reanalysis in terms of Arctic processes, low ozone levels at low latitudes, and pollution transport

Yugo Kanaya[1], Kazuyuki Miyazaki[2,1], Fumikazu Taketani[1], Takuma Miyakawa[1], Hisahiro Takashima[1,3], Yuichi Komazaki[1], Xiaole Pan[1,4], Saki Kato[3], Kengo Sudo[1,5], Takashi Sekiya[1], Jun Inoue[6], Kazutoshi Sato[7], and Kazuhiro Oshima[1,8]

[1] Japan Agency for Marine–Earth Science and Technology (JAMSTEC), Yokohama 2360001 Japan
[2] Jet Propulsion Laboratory, California Institute of Technology, Pasadena 91109, CA, USA
[3] Fukuoka University, Fukuoka 8140133, Japan
[4] Now at Institute of Atmospheric Physics, Chinese Academy of Sciences, Beijing 100029, China
[5] Nagoya University, Nagoya 4648601, Japan
[6] National Institute of Polar Research, Tachikawa 1908518, Japan
[7] Kitami Institute of Technology, Kitami 0908507, Japan
[8] Now at Institute of Environmental Sciences, Rokkasho 0393212, Japan

Correspondence to: Yugo Kanaya (yugo@jamstec.go.jp)

Abstract. Constraints from ozone (O_3) observations over oceans are needed in addition to those from terrestrial regions to fully understand global tropospheric chemistry and its impact on the climate. Here, we provide a large data set of ozone and carbon monoxide (CO) levels observed (for 11 666 and 10 681 h, respectively) over oceans. The data set is derived from observations made during 24 research cruise legs of R/V *Mirai* during 2012 to 2017, in the Southern, Indian, Pacific, and Arctic Oceans, covering the region from 67° S to 75° N. The data are suitable for critical evaluation of the over-ocean distribution of ozone derived from global atmospheric chemistry models. We first give an overview of the statistics in the data set and highlight key features in terms of geographical distribution and air mass type. We then use the data set to evaluate ozone mixing ratio fields from the Tropospheric Chemistry Reanalysis version 2 (TCR-2), produced by assimilating a suite of satellite observations of multiple species into a global atmospheric chemistry model, namely CHASER. For long-range transport of polluted air masses from continents to the oceans, during which the effects of forest fires and fossil fuel combustion were recognized, TCR-2 gave an excellent performance in reproducing the observed temporal variations and photochemical buildup of O_3 when assessed from $\Delta O_3/\Delta CO$ ratios. For clean marine conditions with low and stable CO mixing ratios, two focused analyses were performed. The first was in the Arctic (>70° N) in September every year from 2013 to 2016; TCR-2 underpredicted O_3 levels by 6.7 ppbv (21 %) on average. The observed vertical profiles from O_3 soundings from R/V *Mirai* during September 2014 had less steep vertical gradients at low altitudes (>850 hPa) than those obtained by TCR-2. This suggests the possibility of more efficient descent of the O_3-rich air from above than assumed in the models. For TCR-2 (CHASER), dry deposition on the Arctic ocean surface might also have been overestimated. In the

second analysis, over the western Pacific equatorial region (125–165° E, 10° S to 25° N), the observed O_3 level more frequently decreased to less than 10 ppbv in comparison to that obtained with TCR-2, and also those obtained in most of the Atmospheric Chemistry Climate Model Intercomparison Project (ACCMIP) model runs for the decade from 2000. These results imply loss processes that are unaccounted for in the models. We found that the model's positive bias positively correlated with the daytime residence times of air masses over a particular grid, namely 165–180° E and 15–30° N; an additional loss rate of 0.25 ppbv h^{-1} in the grid best explained the gap. Halogen chemistry, which is commonly omitted from currently used models, might be active in this region and could have contributed to additional losses. Our open data set covering wide ocean regions is complementary to the Tropospheric Ozone Assessment Report data set, which basically comprises ground-based observations, and enables a fully global study of the behavior of O_3.

1 Introduction

The global burden and distribution of tropospheric ozone (O_3) have changed from preindustrial times to the present, and have induced radiative forcing of $+0.4 \pm 0.2$ W m^{-2} (IPCC, 2013) by interactions with the Earth's radiative field. The distribution of O_3 is critical for determining concentration fields of hydroxyl radicals, which control the lifetimes of many important chemical species, including methane. Changes in atmospheric chemistry and their impacts on the climate are often investigated by using O_3 distributions derived from global atmospheric chemistry model simulations. Therefore the model performance determines the accuracy of the assessment, requiring model evaluation against field observations of levels of O_3 and its precursors. For example, the models included in the Atmospheric Chemistry Climate Model Intercomparison Project (ACCMIP; Lamarque et al., 2013; Shindell et al., 2011) and the Chemistry–Climate Model Initiative (CCMI; Morgenstein et al., 2017) were carefully evaluated against field observations (e.g., Tilmes et al., 2016). Recently, an unprecedented comprehensive data set of O_3 measurements was systematically compiled under a community-wide activity, i.e., the Tropospheric Ozone Assessment Report (TOAR) (Cooper et al., 2014; Schultz et al., 2017; Gaudel et al., 2018), and this provided additional constraints for model simulations.

However, even with the data in the TOAR, observation data coverage over oceans is still poor; Schultz et al. (2017) reported that the 'true oceanic sites' covered by TOAR were American Samoa (14.25° S, 170.56° W), Sable Island (43.93° N, 59.90° W), the Ieodo Ocean Research Station (32.12° N, 125.18° E), Ogasawara (27.08° N, 142.22° E), and Minamitorishima (24.28° N, 153.98° E), while Cape Grim (40.68° S, 144.69° E), Amsterdam Island (37.80° S, 77.54° E), and Mace Head (53.33° N, 9.90° W) were also included in other categories. For assessment of the Arctic region (AMAP, 2015), observations obtained truly over the Arctic Ocean were largely unavailable; only observations at costal or inland sites such as Alert (82.45° N, 62.51° W), Barrow (71.32° N, 156.61° W), Zeppelin (78.90° N, 11.88° E), Pallas–Sodankyla (67.97° N, 24.12° E), Summit, (72.58° N, 38.46° W) and Thule (76.5° N, 68.8° W) were used to test simulations. Measurements from individual cruises (e.g., Boylan et al., 2015; Dickerson et al., 1999; Kobayashi et al., 2008; Prados-

Roman et al., 2015), a large collection from multiple cruises (e.g., Lelieveld et al., 2004), O_3 soundings from the SHADOZ network (e.g., Thompson et al., 2017; Oltmans et al., 2001), and those from various campaigns (e.g., Kley et al., 1996; Takashima et al., 2008; Rex et al., 2014) have provided important O_3 data over oceanic regions. However, their spatio-temporal coverage over open oceans is too sparse to complete the global picture. Aircraft observations (e.g., HIAPER Pole-to-Pole Observations (HIPPO); Wofsy et al., 2011) also sampled marine boundary layer but the measurement frequency was not necessarily high. One mature example of such global observations that include the over-ocean atmosphere is that for CO_2. For example, observational data at a large number of remote islands are available from the World Data Centre for Greenhouse Gases (WDCGG) database of the World Meteorological Organization (WMO)/GAW. Atmospheric CO_2 measurements are now accepted by SOCAT Version 4 (https://www.socat.info/), which is a database of ship-based observations, e.g., from research vessels and voluntary ships. Similarly dense O_3 observations over oceans are needed.

An understanding of the processes behind the O_3 mixing ratio distribution is important. Young et al. (2018) reported that the rates of chemical processes (production and loss) and deposition/stratosphere–troposphere exchange could differ among models by factors of 2–3. More observational constraints for characterizing photochemical buildup and long-range transport events using tracers such as carbon monoxide (CO) are required. The chemical loss term under clean marine conditions should also be examined; the loss rate caused by halogen chemistry, and the regions where such chemistry is important, need to be evaluated.

Since 2010, we have conducted ship-borne observations on R/V *Mirai* of the atmospheric composition, including the O_3 and CO levels, for more than 10 000 h. The geographical coverage was wide, namely the Arctic, Pacific, Indian, and Southern Oceans. Such observations, together with currently available data sets, will enable critical testing of model simulations that cover the entire globe. In this paper, we present our observational data set for O_3 and CO for the first time. The data were separately analyzed for cases affected by long-range transport and those under clean marine conditions. For each case, the observations were compared with independent reanalysis data from Tropospheric Chemistry Reanalysis version 2 (TCR-2). The aims are to interpret the observations and to evaluate the reanalysis data over the oceans. The reanalysis data were produced by assimilating a suite of satellite data for O_3 and precursors into a global atmospheric chemistry model, namely CHASER. The precursor emissions were simultaneously optimized. This has advantages over forward model simulations incorporating a bottom-up emission inventory because realistic emissions are taken into account, even those for recent years, for which a bottom-up emission inventory is not yet ready. TCR-2 was updated from the previous version TCR-1 (Miyazaki et al., 2015); the spatial resolution has been improved and newer satellite products are used for assimilation. For TCR-1, evaluation against surface, sonde, and aircraft observations was successful (Miyazaki et al., 2015; Miyazaki and Bowman, 2017). For TCR-2, the performance has been evaluated using the KORUS-AQ aircraft campaign measurements over East Asia (Miyazaki et al., 2019). However, insufficient evaluation against data over remote oceans has been performed and our motivation in this study was to attempt this.

In Sect. 2, field observations and the assimilation model are outlined. In Sect. 3, geographical and statistical overviews of the observational data are presented and then compared with the data from TCR-2. CO data and backward trajectories are

used to classify O_3 data into cases that are influenced by long-range transport of pollution from continents and other cases, namely clean remote air masses. For the former cases, the reproducibility of the O_3 mixing ratio levels and whether the chemical buildup is well reproduced by the reanalysis were tested for more than 20 events. For the latter cases, a particular focus was placed on underestimation for the Arctic Ocean and overestimation for the western Pacific equatorial region by

5   TCR-2. Similar trends were observed with the ensemble median of model runs of ACCMIP. Possible explanations for these discrepancies were investigated.

2 Methodology

2.1 Observations on R/V *Mirai*

    Atmospheric composition observations were conducted on R/V *Mirai* (8706 gross tons) of the Japan Agency for Marine–

10   Earth Science and Technology (JAMSTEC) from 2010. The O_3 and CO levels were determined by UV and IR absorption methods (Models 49C and 48C, Thermo Scientific, Waltham, MA, USA), respectively. The instruments were located in an observational room on the top floor. Two Teflon tubes (6.35 mm o.d.) of length ~20 m were used to sample air near the bow to best avoid contamination from the ship's exhaust. The exhaust effect was clearly discerned in the 1 min O_3 data record as high concentrations of NO in the exhaust titrated O_3. Minute data exceeding 3-sigma of the standard deviation in an hour

15   were eliminated before producing hourly averages. The CO data for the same minutes were removed. The CO instrument alternately measured the ambient (for 40 min) and zero (for 20 min) levels. For the zero-level observations, CO was removed from the ambient air by using a zero-air generator equipped with a heated Pt catalyst (Model 96, Nippon Thermo, Uji, Japan). The O_3 instrument was calibrated twice per year in the laboratory, before and after deployment, using a primary standard O_3 generator (Model 49PS, Thermo Scientific, Waltham, MA, USA). The CO instrument was calibrated on board twice per year,

20   on embarking and disembarking of the instrument, using a premixed standard gas (CO/N_2, 1.02 ppm, Taiyo-Nissan, Tokyo, Japan). The reproducibility of the calibration was to within 1 % for O_3 and 3 % for CO.

    The 24 cruise legs during which the two instruments were operated are listed in Table 1. During MR12-02 Legs 1 and 2, the CO instrument did not work well and only the O_3 data were used for analysis. The cruise regions ranged widely, from the Arctic, the North, equatorial, and South Pacific Ocean, the eastern part of the Indian Ocean, to the Southern Ocean. The

25   Arctic cruises took place every year during the period 2013 to 2016 (specifically during the MR13-06, 14-05, 15-03, and 16-06 cruises). Other cruises aimed to study geology, meteorology, and oceanography, and took place in the Pacific, Indian, and Southern Oceans. The western Pacific equatorial region and Indian Oceans were also frequently visited for operation of the TRITON buoy. Regions near Japan were frequently observed because the departure/arrival ports were often in that country. Our data basically did not include observations made while the vessel was anchored in ports; exceptions were the inclusion

30   of short on-port data when the ports were visited during cruise legs (see the far-right-hand column in Table 1). During many cruises, other instruments, i.e., for performing black carbon and fluorescent aerosol measurements, and multi-axis

differential optical absorption spectroscopy (MAX-DOAS), were operated together (e.g., Taketani et al., 2016; Takashima et al., 2016). These data will be reported in future publications.

2.2 Reanalysis and ACCMIP models

The first version of tropospheric chemistry reanalysis from JAMSTEC, i.e., TCR-1, which used an ensemble Kalman filter
5 (EnKF) approach with a global atmospheric chemistry model (CHASER) as a base forward model, has been previously described (Miyazaki et al., 2015). Here, the updated version, TCR-2, was used (Miyazaki et al., in preparation, 2019, https://ebcrpa.jamstec.go.jp/tcr2/about_data.html). The detailed description of the basic data assimilation framework and the evaluation results using the KORUS-AQ aircraft measurements over East Asia are available in Miyazaki et al. (2019), while detailed global evaluations are ongoing. The major aspects of the update of TCR-1 were a finer horizontal resolution (1.1°,
10 compared with 2.8° in TCR-1), assimilation of newer satellite data products [OMI NO_2 (QA4ECV), GOME-2 NO_2 (TM4NO2A v2.3), TES O_3 (v6), MOPITT CO (v7 NIR), and MLS O_3, NO_3 (v4.2)], and extension of the period to 2017 (from 2005). A priori emissions were obtained from EDGAR v4.2 for anthropogenic sources, GFED v3.1 for open-fire emissions, and GEIA for biogenic sources. In addition to concentration fields of chemical species, NO_x emissions (surface and lightning, separately) and CO were included in the state vector and were simultaneously optimized. An advantage was
15 that analysis for recent years (e.g., 2017) was possible before development of a bottom-up emission inventory. The base forward model CHASER V4.0 used for TCR-2 has been described by Sekiya et al. (2018). Briefly, 93 species and 263 reactions (including heterogeneous reactions) represent O_x–NO_x–HO_x–CH_4–CO photochemistry and oxidation of non-methane volatile organic compounds. Tropospheric halogen chemistry is not included. The dry deposition velocity (v_d) of O_3 was computed as $(r_a + r_b + r_s)^{-1}$, where r_a, r_b, and r_s are the aerodynamic resistance, the surface canopy (quasi-laminar) layer
20 resistance, and the surface resistance, respectively (Wesely, 1989). $1/r_s$ over ocean surface was assumed to be 0.075 cm s^{-1} globally, irrespective of regions (Sudo et al., 2002). As a result, v_d was ~0.04 cm s^{-1} over the Arctic open ocean in September, for instance. This will be a subject of discussion in Sect. 3.3.2.

Because the number of assimilated TES O_3 retrievals decreased substantially after 2010, the data assimilation performance became worse after 2010 in the previous version TCR-1 (Miyazaki et al., 2015), and it can be expected that TCR-2 has
25 similar increases in O_3 analysis errors after 2010. Nevertheless, the multi-constituent data assimilation framework provides comprehensive constraints on the chemical system and entire tropospheric O_3 profiles through corrections made to precursors' emissions and stratospheric concentrations, as demonstrated by Miyazaki et al. (2015, 2019).

We also used the monthly ACCMIP ensemble simulations for the present day (Shindell et al., 2011), which were represented as simulation results for a decade from 2000 (Stevenson et al., 2013; Young et al., 2013). The monthly mean O_3
30 field from an ensemble member, MIROC-Chem, with a modeling framework similar to that of TCR-2, provided corresponding climatological mixing ratio levels at a given location. These values were used to evaluate the performance of TCR-2, which uses meteorological data and estimated emissions in those particular years. Seven other ACCMIP ensemble members that provide hourly O_3 mixing ratios at the Earth's surface (CESM-CAM-super fast, CMAM, GEOSCCM, GFDL-

AM3, GISS-E2-R, MOCAGE, and UM-CAM) were also used for comparative analysis, in terms of frequency distribution of O_3 mixing ratios in the Arctic region (domain 1, 72.5–77.5° N, 190–205° E) and in a narrow western Pacific equatorial region (domain 3, 0–15° N, 150–165° E). The ACCMIP results were chosen for the latest intercomparison exercises because the data were publicly available.

<p style="text-align:left">5</p>

2.3 Backward trajectory

Five-day backward trajectories from an altitude of 500 m above sea level (a.s.l.) were calculated every hour from the position of R/V *Mirai* by using NOAA's Hybrid Single-Particle Lagrangian Integrated Trajectory (HYSPLIT) model (Draxler and Rolph, 2013) to trace the origin areas of the observed air masses. GDAS1 three-dimensional meteorological field data with a resolution of 1.0° were used. Cases that did not involve traveling over land regions (at altitudes lower than 2500 m a.s.l.) during the five days were extracted as marine air mass cases. Here, the landmask data from NASA (https://ldas.gsfc.nasa.gov/gldas/data/0.25deg/landmask_mod44w_025.asc) at a resolution of 0.25° were used for making judgments.

3 Results and Discussion

3.1 Overview of geographical distributions of O_3 and CO

Figure 1a shows the entire O_3 data set from observations on R/V *Mirai* from 2012 to 2017. The covered latitudinal range was wide, from 67.00° S (at 06:00 UTC on 16 February 2017 during MR16-09 Leg 3) to 75.12° N (at 06:00 UTC on 6 September 2014 during MR14-05). The highest hourly mixing ratio, i.e. 66.6 ppbv, was recorded twice; first at 35.89° N, 141.95° E, about 70 km east off the coast of the Kanto area, Japan, at 04:00 UTC on 6 July 2012, and secondly at 32.29° N, 146.04° E, about 500 km southeast of the Kanto area at 14:00 UTC on 18 March 2014. During 57 h, the hourly values exceeded 60 ppbv (which corresponds to the environmental standard in Japan) in a similar region off the coast of Japan, under the influence of Asian regional air pollution. The lowest hourly mixing ratio, i.e. 4.3 ppbv, was recorded twice on the western Pacific equatorial region; first at 5.86° N, 156.00° E and secondly at 7.96° N, 156.02° E at 09:00 and 21:00 UTC, respectively, on 11 March 2014. Values lower than 10 ppbv were recorded for a total of 800 h; this will be discussed in the following section.

Figure 2a shows the entire CO data set. The highest mixing ratio was 556 ppbv, which was recorded at 58.00° N, 179.23° E, at 01:00 UTC on 26 September 2016 during the MR16-06 cruise, where a dense plume from severe forest fires in Russia reached as far as the Bering Sea. All 8 h in which the mixing ratio exceeded 500 ppbv were recorded on the same day. There were 59 other hours when the CO mixing ratio exceeded 300 ppbv, when anthropogenic emissions from East Asia and/or biomass burning were important.

Figure 3 shows an example of O_3 variations for data from MR14-06 Leg 1 with backward trajectories. The vessel started from Mutsu port (41.37° N, 141.24° E), stayed for about 32 h at Yokohama port (35.45° N, 139.66° E), and then headed to

the western Pacific equatorial region. A latitudinal gradient was apparent; north of 27° N was dominated by air masses originating from the Asian continent, as shown by violet trajectory lines. During some hours, high levels, i.e., greater than 50 ppbv of O_3, were recorded (points with red trajectory lines). In contrast, marine air masses from the east were dominant south of 27° N and the mixing ratio levels decreased to less than 30 ppbv. South of 15° N, even lower levels were dominant, i.e., <15 ppbv, particularly in equatorial regions where levels less than 10 ppbv of O_3 were frequently observed. The latitudinal gradient, air mass exchange, and transport of photochemically produced O_3 are the three important factors determining distributions. Figure S1 shows the spatial distributions of O_3 and backward trajectories for each cruise leg, and their time series. All three factors listed above for the MR14-06 Leg 1 had major effects on the variations. The classification of air masses as marine and other cases was satisfactory for identifying cases of long-range transport of pollutants from continents, although some events with continental effects with traveling times longer than 120 h were probably wrongly categorized. Because longer trajectories may not be reliable, we will use this criterion (i.e., 120 h) in the following sections with a notice of such limitations. Stratospheric influences were not identified; we did not find any events with reasonable O_3-level enhancement accompanied by descent of air masses from 8 km or higher altitudes within 72 h prior to observations.

3.2 Comparisons between observations and TCR-2 data: Global features

Figures 1b and 2b show the geographical distributions of O_3 and CO obtained from TCR-2 along the cruise track. The nearest grid and time (2 h resolution) at the lowest layer were sampled to achieve the best possible comparison with the observations shown in Figs. 1a and 2a. Most features were in agreement with the observations, in terms of areas with high mixing ratios and latitudinal gradients. This comparison indicates a reasonably high quality of reanalysis data over the oceans. This is partly because the NO_x and CO emissions rates were optimally estimated during the data assimilation cycle and were reflected in the mixing ratio field. The emission changes provide substantial influences on ozone forecasts over many regions. Assimilation of the TES ozone measurements has limited impacts on near surface ozone owing to its weak sensitivity to the lower troposphere.

In Fig. S1, the comparisons are shown as time-series plots. Excellent matches in the evolution with time of O_3 and CO mixing ratios were found for the latter period of MR14-02, i.e., during the period 12–22 March 2014, in the time series (Fig. S1g). The blue lines show plots of monthly climatological mean mixing ratios, which were obtained from MIROC-Chem. Although the monthly means sometimes followed the observed baseline trend for O_3, the performance of TCR-2 was superior, particularly for reproducing detailed peak patterns for CO. This case will be analyzed in Sect. 3.3.1 on photochemical buildup. A similarly excellent performance was obtained for MR15-05 Leg 2 (Fig. S1r) and MR16-09 Leg 4 (Fig. S1w), when the ship returned to Japan from the south.

Clear gaps were also sometimes observed. These are probably related to limited reproducibility in the meteorological field and errors in the emission estimation and other physicochemical processes that were taken into account in the model system. A large gap was observed during the latter half of the MR14-01 cruise (Fig. S1f); the predictions produced by TCR-2 for CO and O_3 in the eastern Indian Ocean were too high. The climatological mean from MIROC-Chem reproduced the observed

level better, which suggests that false information was introduced from satellite observations to the surface mixing ratios, for instance, associated with the use of total column measurements and errors in vertical transport, or that the position of ITCZ was too far south in the simulation. During other cruises, smaller gaps in the peak occurrence times and peak mixing ratio levels were found. For example, during MR14-04 Leg 2 (Fig. S1i), the peak times for O_3 and CO during the period 27 July

5 to 6 August 2014 were out of phase by about one to two days. This was probably caused by a small displacement of pollution air masses after long-range transport. High O_3 mixing ratios, i.e., >70 ppbv (off the scale in the time-series plot) for 23 h were predicted by TCR-2, which was an overestimation compared with the observations. Except for 2 h on 9 October 2014, these were always in July (in 2012, 2013, and 2014). All were found within 200 km east of Japan's main islands, suggesting overestimation of photochemical O_3 production during long-range transport in TCR-2.

10 With such case-dependent reproducibility in mind, Fig. 1c summarizes the overall geographical distribution of the reanalysis/observation ratios for O_3 mixing ratios. For clarity, the data were limited to cases of marine origins, where the differences between the TCR-predicted and observed CO mixing ratios were less than 50 ppbv ($N = 5662$), in contrast to Fig. 1a and b, where all data ($N = 11\ 666$) were included. The model's underestimation in the Arctic Ocean and overestimation over the oceans south of Japan (western Pacific equatorial or subtropical regions) are clearly shown. These features will be

15 discussed in Sect. 3.3.

Figure 4 shows the latitudinal distribution of the observed and TCR-2 O_3 mixing ratios and their ratios. In Fig. 4a, the data were again limited to cases of marine origins, where the differences between the model-derived and observed CO mixing ratios were less than 50 ppbv ($N = 5662$). The variability shown here reflects seasonality and cases of long-range transport from continents over 120 h. The range of TCR-2/observation ratios (shown in red in Fig. 4b) narrowed when TCR-2

20 successfully captured the variability. Data selection ($N = 5662$) also contributed to narrowing of the range (grey points indicate without data selection). The ratios binned by latitudes indicate that TCR-2 tended to give underestimations in high northern latitudes and overestimations in low latitudes. The 10th, 50th (median), and 90th percentiles (range shown as bars) of the ratios at high latitudes (>70° N) were 0.62, 0.81, and 0.94 ($N = 876$); the range was off unity. The medians for low latitudes (0–10° N, 10–20° N, and 20–30° N) were 1.12 ($N = 1061$), 1.28 ($N = 268$), and 1.28 ($N = 195$), respectively.

25 Figure 5 shows a scatterplot of the comparison. The data set was re-expanded by removing the criteria of marine air mass selection and CO differences (i.e., $N = 11\ 666$) to show the overall correlation between the observed and TCR-2 data over the full range. The square of the correlation coefficient (R^2) was 0.59; this increased to 0.62 when clear outliers (latter half of MR14-01 and cases when TCR-2 exceeded 70 ppbv) were omitted (red, $N = 11\ 305$). The excellent performance of TCR-2 was assured by a resolution of 2 h in reproducing O_3 mixing ratio variations. When the data were further binned to a

30 resolution of one day (with observations for 6 h or more), R^2 improved to 0.66; this suggests that the original variability was partly derived from small shifts in the peak times by less than a day. In the past, reanalysis data were not used for such detailed diagnoses, but were normally compared with observations after monthly averaging or binning to coarse latitudinal bands. Recently, Akritidis et al. (2018) evaluated stratosphere-to-troposphere transport processes represented by the Copernicus Atmosphere Monitoring Service (CAMS) system, but evaluation of transport and transformation processes for

tropospheric O_3 over oceans has not been reported with reanalysis. Here, a successful comparison was made for the first time at the daily or finer time-scale. The regression line for the data set, i.e., [TCR-2, ppbv] = $(6.90 \pm 0.15) + (0.71 \pm 0.01) \times$ [obs, ppbv], suggests a statistically significant positive intercept on the y-axis (i.e., TCR-2) and a slope of less than unity. The result was unchanged even when MR14-01 and cases with >70 ppbv in TCR-2 were included. The green circles in Fig. 5 represent data from the Arctic region (>70° N), and clearly suggest an underestimation by TCR-2. In contrast, the blue circles from the western Pacific equatorial region (125–165° E, 10° S to 25° N) fell on the opposite side, with respect to the 1:1 line, indicating an overestimation by TCR-2. These two aspects will be discussed in detail in the following sections.

3.3 Specific analysis with event or regional focuses: Implications for processes

In this section, more detailed comparisons between observations and simulations are made, to shed light on the underlying mechanisms determining O_3 mixing ratio levels and distributions.

3.3.1 Long-range transport events with photochemical production

We selected events with simultaneous increases in CO and O_3 levels or those with at least evident CO peaks. We then assessed the reproducibility of the peak mixing ratios and $\Delta O_3/\Delta CO$ ratios in TCR-2; the $\Delta O_3/\Delta CO$ ratio is an index of the efficiency of photochemical production of O_3 from CO as a precursor. In total, 23 cases were selected (Table 2 and magenta rectangles in Fig. 2a). The two cases discussed below were studied in depth.

Figure 6 shows the time evolution of the O_3 and CO mixing ratios from observations and TCR-2 during the period 16–19 March 2014, when the vessel returned to Japan from the equatorial Pacific during MR14-02. The observational data along the entire track are shown, with the exact position of R/V *Mirai* at that time marked by a black circle. This part of the cruise has already been briefly mentioned in Sect. 3.2; here, the origins of pollution and the photochemical states for three episodes with increased mixing ratios are discussed. First, at 09:00 UTC on 16 March 2014, at 23.69° N, 149.72° E, the CO mixing ratio peaked at around 284 ppbv. The geographical distribution of surface O_3 and CO in TCR-2 implied that this was a tongue-shaped pollution event originating from the Indochina peninsula and extending to the east; however, it was not. Instead, as inferred from the backward trajectories (Fig. S1g), weather charts, and time evolution of CO distributions from TCR-2 (Fig. 6), it should be interpreted as a belt of pollution originating from East Asia, present at the south edge of a high-pressure system moving toward the southeast. An O_3 peak of 54.2 ppbv occurred 10 h later, which was also captured by TCR-2. A second CO peak occurred the next day, at 19:00 UTC on 17 March 2014, at 28.56° N, 147.68° E; in this case an O_3 peak of 66.2 ppbv occurred just 1 h before. TCR-2 suggested that the plume originated from East Asia and was transported to the east from the continent and then to the south, under the influence of another high-pressure system traveling over Japan and a low-pressure system that followed (see the 2nd row panel in Fig. 6 for 01:00 UTC on 17 March 2014). The timing and location of the third peak were also well predicted; a CO peak of 273 ppbv occurred at 17:00 UTC on 18 March 2014, at 32.88° N, 145.77° E, 3 h after the O_3 peak of 66.6 ppbv (the highest in the data set). In this case, the air mass traveled directly from Central East China, with a large precursor emission (see the distribution of grids with high CO

emissions in the panel for 01:00 UTC on 19 March 2014) via a quick westerly flow under the influence of passage of a cold front. The $\Delta O_3/\Delta CO$ ratio, calculated as the slope of the regression line in a scatterplot of hourly mixing ratios of O_3 and CO between 00:00 UTC on 17 March 2014 and 00:00 UTC 19 on March 2014, was 0.11 ± 0.01 ppbv/ppbv ($R = 0.83$) for observations and 0.06 ± 0.01 ppbv/ppbv ($R = 0.75$) for TCR-2 (Table 2, case G). The underestimation of O_3 peaks by TCR-2

5   (maximum 56.3 ppbv) is attributable to a combination of less efficient production of O_3 and underestimation of CO peaks by TCR-2 (maximum 219 ppbv).

Figure 7 shows a similar time evolution during MR14-04 Leg 2, when a plume reached the central Pacific from the Asian continent about 5000 km away. The $\Delta O_3/\Delta CO$ ratio from 00:00 UTC on 2 August 2014 to 00:00 UTC on 4 August 2014 was 0.11 ± 0.01 ppbv/ppbv ($R = 0.90$) for observations and 0.14 ± 0.01 ppbv/ppbv ($R = 0.93$) for TCR-2; the maximum CO and

10   O_3 mixing ratios were 249 and 38.0 ppbv, respectively, for observations, and 220 and 37.2 ppbv, respectively, for TCR-2 (Table 2, case I). The pollution source was probably forest fires in the far east of Russia (shown by plus signs in the upper left panel of Fig. 7) with a smaller contribution from anthropogenic emissions from East Asia. Specifically, on 26 July 2014, the head of a plume extending from the forest fires arrived at northern Japan (see Zhu et al., 2019 and references therein for details) and affected our ship observations. The main body of the plume arrived from the west and traveled with a migrating

15   high-pressure system until 6 August 2014. The observed CO and O_3 mixing ratios decreased during the period 29 July to 1 August 2014, when the vessel was located at the center of a low-pressure system traveling to the east. After the low-pressure system had weakened, the plume was still present in its southern part and was pushed northeast under the influence of the high-pressure system in the south, which again affected the ship observations during 2 and 3 August 2014, in the middle of the North Pacific.

20   Table 2 summarizes the results from all 23 cases, including the two events discussed above (cases F and G from MR14-02 and cases H and I from MR14-04 Leg 2). The span of the study area was from the Indian Ocean in the southern hemisphere, and the central equatorial Pacific Ocean to the Bering Sea (see magenta rectangles in Fig. 2a). In most cases, the observed $\Delta O_3/\Delta CO$ slopes were positive, suggesting photochemical buildup of O_3 with emissions of CO. The ranges were well reproduced by TCR-2. It is interesting to note that negative slopes for $\Delta O_3/\Delta CO$ were found for at least three cases and that

25   these were also well captured by TCR-2. These were the cases where very high CO levels were recorded (479, 358, and 556 ppbv for cases N, S, and T, respectively). The strong negative correlation for case N was influenced by the low O_3 mixing ratios (11.2 ppbv) recorded with high CO levels. When such irregular points were removed, the observed slope was 0.01 ± 0.01 ppbv/ppbv. For case S, a strong CO peak occurred in the south of Japan (~200 km off the coast) on 23 January 2016, without an O_3 increase (Fig. S1r). For case T, a plume from a Russian forest fire affected the observations over the Bering

30   Sea (Fig. S1s). Relatively fresh air pollution from nearby ships or weak UV in January and February for cases N and S, and weak co-emission of NO_x from forest fires for case T, could cause the observed negative slopes. Processes other than daytime photochemistry (e.g., nocturnal chemistry) might also have been important.

Figure 8 shows the correlation between the observed and reanalysis $\Delta O_3/\Delta CO$ ratios. The reasonable correlation, with a slope of 1.15 ± 0.29 and $R^2 = 0.42$, suggests that TCR-2 reproduced the state of O_3 production fairly well for various cases in

different geographical domains in different seasons. Case B is an outlier in terms of correlation; observations and TCR-2 yielded $\Delta O_3/\Delta CO$ ratios of 0.28 ± 0.03 and -0.12 ± 0.06 ppbv/ppbv, respectively. This was recorded at the center of the Bering Sea, where TCR-2 failed to reproduce the coinciding increases in the observed O_3 and CO mixing ratios.

The observed and simulated ranges of the $\Delta O_3/\Delta CO$ ratios are in accordance with previously reported data. On the Azores in the central Atlantic (38.73° N) in spring and on Sable Island (43.93° N) in Atlantic Canada in summer, the $\Delta O_3/\Delta CO$ ratios were uniform, at 0.3−0.4 ppbv/ppbv (Parrish et al., 1998). For TRACE-P aircraft measurements, Hsu et al. (2004) reported smaller values, i.e., 0.08 ppbv/ppbv in the tropics and 0.03 ppbv/ppbv in the extratropics, with CO > 200 ppbv. Weiss-Penzias et al. (2006) reported 0.22 ppbv/ppbv in April and May 2004 for two long-range transport events that reached a mountain on the west coast of the United States from Asia. Tanimoto et al. (2008) summarized the range as being from slightly negative to ~0.4 ppbv/ppbv when observing Siberian fire plumes at Rishiri Island. Zhang et al. (2018) documented the $\Delta O_3/\Delta CO$ ratios at Pico Mountain in the Atlantic Ocean and found that the ratios for anthropogenic pollution were higher (0.45–0.71 ppbv/ppbv) than those for observations affected by wildfires (0.12–0.71 ppbv/ppbv). They suggested that the low ratios from wildfires could be the result of lower NO_x/CO emission ratios compared with those for anthropogenic sources.

3.3.2 Arctic processes

In the Arctic Ocean (>70° N), the CO mixing ratios were regularly close to the background and stable (101 ± 10 ppbv, Fig. S1d, j, n, and s), suggesting that the measurements were not affected by strong pollution events. The average observed O_3 mixing ratio was 31.3 ppbv ($N = 1804$) and the reanalysis significantly underestimated this (24.6 ppbv) based on Welch's t test (p < 0.001). The magnitude of the relationship was common for all four years of measurements (Fig. 9). A low bias with TCR-2 was also clear for cumulative frequency distributions of hourly O_3 mixing ratios from observations (black, $N = 1031$) and TCR-2 (red) in domain 1 [72.5–77.5° N and 190–205° E (155–170° W)] in September (Fig. 10). The frequency distributions for eight model members of ACCMIP and their ensemble median (magenta) are also included in Fig. 10. The median was close to that for TCR-2, and similarly significantly underestimated, although three members (GEOSCCM, GFDL-AM3, and GISS-E2-R) showed better agreement with observations. These analyses suggest that in the simulations, the sources were too weak or the losses were too strong. The average diurnal variations were generally almost flat (the variability was within 5 % of the average) for observations and TCR-2 (not shown), suggesting that the missing processes did not show significant diurnal variability. At high latitudes, the assimilated measurements have either low quality or low sensitivity in the troposphere, while the optimization of precursors emissions generally has limited impacts on ozone. The reanalysis ozone over the Arctic Ocean can be similar to the model predictions, except when poleward transports are strong enough to propagate observational information from low and mid latitudes.

During the MR14-05 cruise, 10 O_3 sondes were launched every other day at 22:00 UTC during the period 6–24 September 2014 (Inoue et al., 2018). The average vertical profile was compared with that from TCR-2 at the nearest grid (Fig. 11), to investigate the altitude to which this low bias of TCR-2 continued. At the lowest altitude near the surface, the underestimation by TCR-2 against the O_3 sonde observations was evident. However, the gap only continued to about 850

hPa, at which the two mixing ratios crossed over, and TCR-2 gave higher mixing ratios at higher altitudes. This suggests that the missing process was only important for the boundary layer, not for the entire troposphere. Inoue et al. (2018) compared the O_3 sonde profiles with ERA-Interim (ERA-I) products, with a focus on troposphere–stratosphere exchange. They found that in the upper troposphere ERA-I had a high bias against observations, similarly to the case for TCR-2; this confirms that the underestimation by the model for the surface did not continue into the tropopause. One possibility is that the model's vertical (downward) mixing near the top of the boundary layer was too weak; this mixing would otherwise have effectively carried the O_3-rich air mass from higher altitudes. Another possibility is that dry deposition on the surface of the Arctic Ocean by the model was too fast. The v_d, ~0.04 cm s^{-1} over the Arctic open ocean in September for CHASER (TCR-2), is on the high side of ~0.01–0.05 cm s^{-1}, a range adopted into global atmospheric chemistry models (see Fig. 4 of Hardacre et al., 2015). Ganzeveld et al. (2009) discussed a sensitivity model run shifting their standard v_d of 0.05 cm s^{-1} to 0.01 cm s^{-1} substantially increased surface ozone concentrations by up to 60% in high-latitude regions.

At Barrow (71.32° N, 156.6° W), the nearest ground-based site, the monthly average O_3 mixing ratios in September were 29.8 and 29.1 ppbv, in 2013 and 2014, respectively (McClure-Begley et al., 2014). These values are close to our observations over oceans, and the model ensemble tended to underestimate mixing ratios in September (AMAP, 2015), similarly to our case.

3.3.3 O_3 levels below 10 ppbv at low latitudes

Figures 1c, 4, and 5 show that TCR-2 tended to overestimate O_3 mixing ratios over the western Pacific equatorial region. For the whole global data set, TCR-2 predicted O_3 levels below 10 ppbv O_3 during 262 h, which is much less than the observed duration, i.e., 800 h. The occurrence frequencies in the region 125–165° E, 10° S to 25° N (defined as domain 2, N = 2258) were large, namely 295 and 205 h for observations and TCR-2 predictions, respectively. When the studied region was further narrowed to 150–165° E and 0–15° N (defined as domain 3, N = 657), the discrepancy increased again, i.e., 199 and 80 h for observations and predictions, respectively. In March and December, observations were frequently conducted in domain 3 (N = 211 and 321, respectively). Figure 12 shows the cumulative relative frequency distributions for observations, and the TCR-2 and ACCMIP models for these two months. In March (Fig. 12a), the observed O_3 mixing ratios in the low ranges (<30th percentiles) were as low as 5 ppbv; these were overestimated by TCR-2. The shape of the distribution was in better agreement for higher ranges (30th to 100th percentiles). The ensemble medians for the ACCMIP runs were higher than the observations for any of the percentiles, whereas CESM-CAM-super fast, GISS-E2-R, GEOSCCM, and MOCAGE better captured features of the observed low mixing ratios (at higher percentiles GEOSCCM and MOCAGE gave too-high mixing ratios). For December (Fig. 12b), the performances of the models were poorer; although CESM-CAM-super fast and GISS-E2-R again captured the observed distributions in low ranges, all others, including the ACCMIP ensemble median and TCR-2, overestimated the mixing ratios for any of the percentiles. The large variations among the model results may reflect the impact of large variations in transport, particularly in March. Because of the lack of direct constraints over the remote

oceans on near surface mixing ratios in the current satellite observing systems, the systematic mismatches imply requirements for exploring model error sources to improve the reanalysis quality.

The average relative diurnal variations normalized to the maximum mixing ratios during these two months (Fig. 13, *x*-axis is UTC + 11 h, adjusted to local time for the selected region) showed a pattern of daytime decreases, suggesting photochemical destruction. However, the observed decrease was stronger (15 %) and earlier than those simulated in the TCR-2 and ACCMIP runs, in which the HO_x cycle was primarily responsible for photochemical destruction. This feature may indicate O_3 loss via a different process, e.g., halogen chemistry, which is not included in any of the model simulations considered in this study.

To obtain further insights into the regions in which this additional loss could be important, the differences between the O_3 levels predicted by TCR-2 and the observed levels were calculated and the correlations with the residence times (in the daytime) of back trajectories in $15° \times 15°$ grid regions around domain 3 were examined. Use of the residence time during the day can be justified because the destruction probably occurred in the daytime (Fig. 13). Figure S2 shows the results for 17 regions, covering 120–195° E and 15° S to 45° N. We found that the residence time in the grid region 165–180° E and 15–30° N, located northeast of domain 3, had the largest positive correlation coefficient (Fig. 14). This suggests that this region is a possible "hot spot" for additional loss. It is worth noting that data from all five cruises contributed to the positive correlation, which suggests that the relationship is reproducible. The slope of the regression line was 0.25 ppbv h^{-1}. This corresponds to the possible loss rate in the grid that best explains the discrepancy between observations and TCR-2 predictions. If the rate is attributed to dry deposition on the sea surface, a deposition velocity as high as 0.33 cm s^{-1} is required, assuming a boundary layer height of 1000 m and an average O_3 mixing ratio of 17.4 ppbv. This high velocity is not supported by previous studies (e.g., Ganzeveld et al., 2009; Hardacre et al., 2015). Such a loss rate can be more easily explained by bromine and/or iodine chemistry in the atmosphere (e.g., Saiz-Lopez et al., 2012, 2014). We observed elevated IO radical concentrations with a MAX-DOAS instrument aboard R/V *Mirai* during the cruises included in the analysis in Fig. 14. Further analysis will be reported in a future publication.

Substantially reduced O_3 levels (<10 ppbv) have been reported in the marine boundary layer over the equatorial Pacific. Johnson et al. (1990) found near-zero (3 ppbv or less) O_3 mixing ratios in the central equatorial Pacific during April and May. Kley et al. (1996) observed similar events in March 1993, with mixing ratios occasionally reaching 3–5 ppbv, from O_3 soundings in a region between the Solomon Islands (9.4° S, 160.1° E) and Christmas Island (2° N, 157.5° W). Takashima et al. (2008) reported substantially reduced O_3 events throughout the year on Christmas Island. Rex et al. (2014) used a combination of O_3 sounding data from the TransBrom cruise of R/V *Sonne* in October 2009, atmospheric chemistry models, and satellite observations to identify a region with strong O_3 depletion in the marine boundary layer at 0–10° N along the north–south cruise track (at around 150° E). This is in good agreement with our observations. Hu et al. (2010) reported that average O_3 mixing ratios at Kwajalein Island (8.72° N, 167.73° E), Republic of the Marshall Islands, located near our "hot spot" grid, during July, August, and September 1999, were lower than 10 ppbv throughout 24 h, with an afternoon decrease of about 1 ppbv. Gómez Martín et al. (2016) reported year-round continuous observations of surface O_3 at San Cristóbal

(0.90° S, 89.61° W) and at Puerto Villamil, Isabela Island (0.96° S, 90.97° W), in the Galápagos Islands in the equatorial eastern Pacific. Daily averages as low as 5–6 ppbv were observed during the period February to May. During the Malaspina circumnavigation in 2010, O_3 mixing ratios as low as 3.4 ppbv were detected around the central Pacific equatorial region (Prados-Roman et al., 2015). During PEM-West A in October 1991, Singh et al. (1996) reported O_3 levels as low as 8–9

5 ppbv from aircraft measurements at altitudes of 0.3–0.5 km in the region 0–20° N in the western and central Pacific. It is worth noting that the O_3 levels over the Atlantic were typically higher, e.g., 30–35 ppbv (Read et al., 2008), even when halogen-mediated destruction was considered. In these studies, detailed statistical comparisons of the observed O_3 levels with chemistry-climate model simulations or reanalysis data as focused here have not been achieved. Conducting continuous observations of O_3 during a large number of cruise legs was useful for obtaining a large data set for performing detailed

10 statistical analysis.

The influence of halogen (bromine and/or iodine) chemistry on O_3 levels has been studied using model simulations at assumed (e.g., Davis et al., 1996; Hu et al., 2010) and observed levels of halogen compounds (Mahajan et al., 2012; Großmann et al., 2013; Dix et al., 2013; Prados-Roman et al., 2015; Koenig et al., 2017) over the Pacific. For example, for bromine chemistry, Hu et al. (2010) estimated a photochemical loss rate of up to 0.12 ppbv h^{-1}. A loss of about 0.4 ppbv d^{-1}

15 can be attributed to halogen chemistry in the marine boundary layer south of Hawaii (Dix et al., 2013). From CAM-Chem-based global model simulations, Saiz-Lopez et al. (2012) estimated an annually integrated rate of surface O_3 loss through halogen chemistry as ~0.15 ppbv h^{-1} in the daytime, over the region 20° S to 20° N. On the basis of GEOS-Chem, Sherwen et al. (2016) suggested that halogen chemistry would reduce surface O_3 levels by ~3–5 ppbv over our domain 3. These loss rates caused by halogen chemistry are in fair agreement with the required additional loss rate, i.e., ~0.25 ppbv h^{-1}, estimated

20 in this study.

Our observational O_3 data set with a large geographical coverage will be useful for evaluating up-to-date model simulations with inclusion of halogen chemistry. Analysis at mid-latitude regions over the Pacific are also of interest because the importance of halogen chemistry in this region has been indicated (e.g., Nagao et al. 1999; Galbally et al. 2000; Watanabe et al., 2005).

25 **4 Summary and outlook**

We compiled a large data set of shipborne in situ observations of O_3 and CO levels with a 1 h resolution, which were recorded on R/V *Mirai* over the Arctic, Bering, Pacific, Indian, and Southern Oceans from 67° S to 75° N, during the period 2012 to 2017. We used the data set to evaluate tropospheric chemistry reanalysis data from TCR-2 and ACCMIP model simulations. TCR-2 captured the basic features of the observations, including the latitudinal gradient and air mass exchange,

30 and therefore enabled interpretation of observations regarding transport and pollution sources. Correlations with observations were sufficient (R^2 up to 0.62 for hourly data and 0.67 for daily data). This suggests an excellent performance by TCR-2 in representing the temporal and geographical distributions of surface O_3. For over 23 long-range transport events with CO

and/or O_3 buildup, variations in the $\Delta O_3/\Delta CO$ ratios were well reproduced by TCR-2. This suggests that the nature of photochemical evolution during transport of pollution plumes was also well captured. However, two major discrepancies were identified; in the Arctic (>70° N) in September, TCR-2 and the ensemble median of model runs of ACCMIP tended to underestimate O_3 levels. From analysis of O_3 sonde measurements, we concluded that the gap was related to processes relevant to the boundary layer; downward mixing from the free troposphere, with a higher O_3 abundance, might have been too weak in the models. For TCR-2, dry deposition on the Arctic Ocean surface might have been too fast. Conversely, in the western Pacific equatorial region, TCR-2 and ACCMIP simulations significantly overestimated the observed O_3 levels, which were often less than 10 ppbv. The minimum in the observed diurnal pattern occurred earlier than those in the models. The gap of mixing ratios correlated with the residence time of trajectories over a particular grid, i.e., 165–180° E and 15–30° N. These analyses indicate the importance of halogen chemistry, which is not accounted for in the models, and the region in which it is active. The data set from our observations (which will continue) is open and complements the TOAR data collection and will be useful for critically evaluating global-scale atmospheric chemistry model simulations, including those from CCMI, AerChemMIP (Collins et al., 2017), and future intermodel comparisons.

Data availability

The observational data set for O_3 and CO obtained on R/V *Mirai* for the study period (2012–2017) is collectively available from https://ebcrpa.jamstec.go.jp/atmoscomp/obsdata/ as a single text file and from http://www.godac.jamstec.go.jp/darwin/e for individual cruise legs. TCR-2 reanalysis data are available from http://ebcrpa.jamstec.go.jp/tcr2/download.html.

Author contribution

YK (Kanaya) designed the study, conducted analyses, wrote the manuscript, managed the instruments and created the observational data set. KM, TS and KS (Sudo) created TCR-2 data. FT, TM, HT, YK (Komazaki), XP and SK substantially contributed to shipborne observations and preparation. HT and SK also provided supporting data from MAX-DOAS observations. JI, KS (Sato) and KO conducted shipborne ozone soundings and provided the data. All co-authors provided professional comments to improve the manuscript.

Competing interest

The authors declare that they have no conflict of interest.

Acknowledgments

We gratefully acknowledge assistance from the Principal Investigators of all cruises and support from Global Ocean Development Inc. and Nippon Marine Enterprise, Ltd. This research was supported by the Coordination Funds for Promoting AeroSpace Utilization and by the Arctic Challenge for Sustainability (ArCS) project of the Ministry of Education, Culture, Sports, Science and Technology (MEXT), MEXT/JSPS KAKENHI Grant Numbers 24241009, 18H04143 and 18H01285, and the Environment Research and Technology Development Fund (2-1803) of the Ministry of the Environment, Japan. Part of the research was carried out at the Jet Propulsion Laboratory, California Institute of Technology, under a contract with the National Aeronautics and Space Administration. We thank Helen McPherson, PhD, from Edanz Group (www.edanzediting.com/ac) for editing a draft of this manuscript.

References

Akritidis, D., Katragkou, E., Zanis, P., Pytharoulis, I., Melas, D., Flemming, J., Inness, A., Clark, H., Plu, M., and Eskes, H.: A deep stratosphere-to-troposphere ozone transport event over Europe simulated in CAMS global and regional forecast systems: analysis and evaluation, Atmos. Chem. Phys., 18, 15515-15534, https://doi.org/10.5194/acp-18-15515-2018, 2018.

Arctic Monitoring and Assessment Programme (AMAP), AMAP Assessment 2015: Black carbon and ozone as Arctic climate forcers. Arctic Monitoring and Assessment Programme (AMAP), Oslo, Norway. vii + 116 pp.

Boylan, P., Helmig, D., Oltmans, S.: Ozone in the Atlantic Ocean marine boundary layer. Elem Sci Anth., 3, p.000045, DOI: http://doi.org/10.12952/journal.elementa.000045, 2015.

Collins, W. J., Lamarque, J.-F., Schulz, M., Boucher, O., Eyring, V., Hegglin, M. I., Maycock, A., Myhre, G., Prather, M., Shindell, D., and Smith, S. J.: AerChemMIP: quantifying the effects of chemistry and aerosols in CMIP6, Geosci. Model Dev., 10, 585-607, https://doi.org/10.5194/gmd-10-585-2017, 2017.

Cooper, O. R., Parrish, D. D., Ziemke, J., Balashov, N. V., Cupeiro, M., Galbally, I. E., Gilge, S., Horowitz, L., Jensen, N. R., Lamarque, J.-F., Naik, V., Oltmans, S. J., Schwab, J., Shindell, D. T., Thompson, A. M., Thouret, V., Wang, Y., and Zbinden, R. M.: Global distribution and trends of tropospheric ozone: An observation-based review, Elem Sci Anth, 2, p.000029, DOI: http://doi.org/10.12952/journal.elementa.000029, 2014.

Davis, D., Crawford, J., Liu, S., McKeen, S., Bandy, A., Thornton, D., Rowland, F., and Blake, D.: Potential impact of iodine on tropospheric levels of ozone and other critical oxidants, J. Geophys. Res., 101, 2135, doi:10.1029/95JD02727, 1996.

Dickerson, R. R., Rhoads, K. P., Carsey, T. P., Oltmans, S. J., Burrows, J. P., and Crutzen, P. J.: Ozone in the remote marine boundary layer: A possible role for halogens, J. Geophys. Res., 104(D17), 21385–21395, doi: 10.1029/1999JD900023, 1999.

Dix, B., Baidar, S., Bresch, J. F., Hall, S. R., Schmidt, K. S., Wang, S., and Volkamer, R.: Detection of IO in the tropical FT, Proceedings of the National Academy of Science, 110 (6), 2035-2040; DOI: 10.1073/pnas.1212386110, 2013

Draxler, R R., and Rolph, G. D.: HYSPLIT (HYbrid Single-Particle Lagrangian Integrated Trajectory) Model access via NOAA ARL READY Website (http://www.arl.noaa.gov/HYSPLIT.php). NOAA Air Resources Laboratory, College Park, MD, 2013.

Galbally, I. E., Bentley, S. T., and Meyer, C. P. (Mick): Mid-latitude marine boundary layer ozone destruction at visible sunrise observed at Cape Grim, Tasmania, 41°S, Geophys. Res. Lett., 27(23), https://doi.org/10.1029/1999GL010943, 2000.

Ganzeveld, L., Helmig, D., Fairall, C. W., Hare, J., and Pozzer, A.: Atmosphere-ocean ozone exchange: A global modeling study of biogeochemical, atmospheric, and waterside turbulence dependencies, Global Biogeochem. Cy., 23, GB4021, doi:10.1029/2008GB003301, 2009.

Gaudel, A., Cooper, O. R., Ancellet, G., Barret, B., Boynard, A., Burrows, J. P., Clerbaux, C., Coheur, P.-F., Cuesta, J., Cuevas, E., Doniki, S., Dufour, G., Ebojie, F., Foret, G., Garcia, O., Granados-Muñoz, M. J., Hannigan, J. W., Hase, F., Hassler, B., Huang, G., Hurtmans, D., Jaffe, D., Jones, N., Kalabokas, P., Kerridge, B., Kulawik, S., Latter, B., Leblanc, T., Le Flochmoën, E., Lin, W., Liu, J., Liu, X., Mahieu, E., McClure-Begley, A., Neu, J. L., Osman, M., Palm, M., Petetin, H., Petropavlovskikh, I., Querel, R., Rahpoe, N., Rozanov, A., Shultz, M. G., Schwab, J., Siddans, R., Smale, D., Steinbacher, M., Tanimoto, H., Tarasick, D. W., Thouret, V., Thompson, A. M., Trickl, T., Weatherhead, E., Wespes, C., Worden, H. M., Vigouroux, C., Xu, X., Zeng, G., and Ziemke, J.: Tropospheric Ozone Assessment Report: Present day distribution and trends of tropospheric ozone relevant to climate and global atmospheric chemistry model evaluation. Elem Sci Anth, 6(1), p.39. DOI: http://doi.org/10.1525/elementa.291, 2018.

Großmann, K., Frieß, U., Peters, E., Wittrock, F., Lampel, J., Yilmaz, S., Tschritter, J., Sommariva, R., von Glasow, R., Quack, B., Krüger, K., Pfeilsticker, K., and Platt, U.: Iodine monoxide in the Western Pacific marine boundary layer, Atmos. Chem. Phys., 13, 3363-3378, https://doi.org/10.5194/acp-13-3363-2013, 2013.

Gómez Martín, J. C., Vömel, H., Hay, T. D., Mahajan, A. S., Ordóñez, C., Parrondo Sempere, M. C., Gil-Ojeda, M., and Saiz-Lopez, A.: On the variability of ozone in the equatorial eastern Pacific boundary layer, J. Geophys. Res. Atmos., 121, 11,086–11,103, doi: 10.1002/2016JD025392, 2016.

Hardacre, C., Wild, O., and Emberson, L.: An evaluation of ozone dry deposition in global scale chemistry climate models, Atmos. Chem. Phys., 15, 6419-6436, https://doi.org/10.5194/acp-15-6419-2015, 2015.

Hsu, J., Prather, M. J., Wild, O., Sundet, J. K., Isaksen, I. S. A., Browell, E. V., Avery, M. A., and Sachse, G. W.: Are the TRACE-P measurements representative of the western Pacific during March 2001? J. Geophys. Res., 109, D02314, doi: 10.1029/2003JD004002, 2004.

Hu, X.-M., Sigler, J. M., and Fuentes, J. D.: Variability of ozone in the marine boundary layer of the equatorial Pacific Ocean, J. Atmos. Chem., 66, 117-136, 2010.

Inoue, J., Sato, K., and Oshima, K.: Comparison of the Arctic tropospheric structures from the ERA-Interim reanalysis with in situ observations, Okhotsk Sea and Polar Research, 2, 7-12, 2018.

IPCC: Climate Change 2013: The Physical Science Basis, Cambridge University Press, Cambridge, United Kingdom and New York, NY, USA, 2013.

Johnson, J. E., Richard H., Gammon, Larsen, J., Bates, T. S., Oltmans, S. J., and Farmer, J. C.: Ozone in the marine boundary layer over the Pacific and Indian oceans: Latitudinal gradients and diurnal cycles, J. Geophys. Res., **95**, 11847-11856 ,1990.

Kley, D., Crutzen, P. J., Smit, H. G. J., Vomel, H., Oltmans, S. J., Grassl, H., and Ramanathan, V.: Observations of near-zero ozone levels over the convective Pacific: effects on air chemistry. Science 274, 230–233, 1996.

Kobayashi, K., Hiraki, T., and Ishida, H.: Ozone concentrations in the surface atmosphere over the Western Pacific Ocean in summer and winter, Kankyo-Gijutsu, 37(5), 332, https://www.jstage.jst.go.jp/article/jriet/37/5/37_5_332/_pdf/-char/ja, 2008. (Japanese with English abstract)

Lamarque, J.-F., Shindell, D. T., Josse, B., Young, P. J., Cionni, I., Eyring, V., Bergmann, D., Cameron-Smith, P., Collins, W. J., Doherty, R., Dalsoren, S., Faluvegi, G., Folberth, G., Ghan, S. J., Horowitz, L. W., Lee, Y. H., MacKenzie, I. A., Nagashima, T., Naik, V., Plummer, D., Righi, M., Rumbold, S. T., Schulz, M., Skeie, R. B., Stevenson, D. S., Strode, S., Sudo, K., Szopa, S., Voulgarakis, A., and Zeng, G.: The Atmospheric Chemistry and Climate Model Intercomparison Project (ACCMIP): overview and description of models, simulations and climate diagnostics, Geosci. Model Dev., 6, 179-206, https://doi.org/10.5194/gmd-6-179-2013, 2013.

Lelieveld, J., Van Aardenne, J., Fischer, H., De Reus, M., Williams, J. and Winkler, P., 2004. Increasing ozone over the Atlantic Ocean. Science, 304(5676), 1483-1487.

Mahajan, A. S., Gómez Martín, J. C., Hay, T. D., Royer, S.-J., Yvon-Lewis, S., Liu, Y., Hu, L., Prados-Roman, C., Ordóñez, C., Plane, J. M. C., and Saiz-Lopez, A.: Latitudinal distribution of reactive iodine in the Eastern Pacific and its link to open ocean sources, Atmos. Chem. Phys., 12, 11609-11617, https://doi.org/10.5194/acp-12-11609-2012, 2012.

McClure-Begley, A., Petropavlovskikh, I., and Oltmans, S.: NOAA Global Monitoring Surface Ozone Network. 1973-2014. National Oceanic and Atmospheric Administration, Earth Systems Research Laboratory Global Monitoring Division. Boulder, CO. http://dx.doi.org/10.7289/V57P8WBF, 2014.

Miyazaki, K. and Bowman, K.: Evaluation of ACCMIP ozone simulations and ozonesonde sampling biases using a satellite-based multi-constituent chemical reanalysis, Atmos. Chem. Phys., 17, 8285-8312, https://doi.org/10.5194/acp-17-8285-2017, 2017.

Miyazaki, K., Eskes, H. J., and Sudo, K.: A tropospheric chemistry reanalysis for the years 2005–2012 based on an assimilation of OMI, MLS, TES, and MOPITT satellite data, Atmos. Chem. Phys., 15, 8315-8348, https://doi.org/10.5194/acp-15-8315-2015, 2015.

Miyazaki. K., Sekiya, T., Fu, D., Bowman, K. W., Kulawik, S. S., Sudo, K., Walker, T., Kanaya, Y., Takigawa, M., Ogochi, K., Eskes, H., Boersma, K. F., Thompson, A. M., Gaubert, B., Barre, J., and Emmons, L. K.: Balance of emission and dynamical controls on ozone during KORUS-AQ from multi-constituent satellite data assimilation, J. Geophys. Res., 124, 387– 413. https://doi.org/10.1029/2018JD028912, 2019.

Morgenstern, O., Hegglin, M. I., Rozanov, E., O'Connor, F. M., Abraham, N. L., Akiyoshi, H., Archibald, A. T., Bekki, S., Butchart, N., Chipperfield, M. P., Deushi, M., Dhomse, S. S., Garcia, R. R., Hardiman, S. C., Horowitz, L. W., Jöckel, P., Josse, B., Kinnison, D., Lin, M., Mancini, E., Manyin, M. E., Marchand, M., Marécal, V., Michou, M., Oman, L. D., Pitari, G., Plummer, D. A., Revell, L. E., Saint-Martin, D., Schofield, R., Stenke, A., Stone, K., Sudo, K., Tanaka, T. Y., Tilmes, S., Yamashita, Y., Yoshida, K., and Zeng, G.: Review of the global models used within phase 1 of the Chemistry–Climate Model Initiative (CCMI), Geosci. Model Dev., 10, 639-671, https://doi.org/10.5194/gmd-10-639-2017, 2017.

Nagao, I., Matsumoto, K., and Tanaka, H.: Sunrise ozone destruction found in the sub-tropical marine boundary layer, Geophys. Res. Lett., 26, 3377-3380, 1999.

Oltmans, S. J., Johnson, B. J., Harris, J. M., Vömel, H., Thompson, A. M., Koshy, K., Simon, P., Bendura, R. J., Logan, J. A., Hasebe, F., Shiotani, S., Kirchhoff, V. W. J. H., Maata, M., Sami, G., Samad, A., Tabuadravu, J., Enriquez, H., Agama, M., Cornejo, J., Paredes F.: Ozone in the Pacific tropical troposphere from ozonesonde observations, J. Geophys. Res., 106(D23), 32503–32525, doi: 10.1029/2000JD900834, 2001.

Parrish, D. D., Trainer, M., Holloway, J. S., Yee, J. E., Warshawsky, M. S., and Fehsenfeld, F. C.: Relationship between ozone and carbon monoxide at surface sites in the North Atlantic region, J. Geophys. Res., 103(D11), 13357-13376,1998.

Prados-Roman, C., Cuevas, C. A., Hay, T., Fernandez, R. P., Mahajan, A. S., Royer, S.-J., Galí, M., Simó, R., Dachs, J., Großmann, K., Kinnison, D. E., Lamarque, J.-F., and Saiz-Lopez, A.: Iodine oxide in the global marine boundary layer, Atmos. Chem. Phys., 15, 583-593, https://doi.org/10.5194/acp-15-583-2015, 2015.

Read, K. A., Mahajan, A. S., Carpenter, L. J., Evans, M. J., Faria, B. V. E., Heard, D. E., Hopkins, J. R., Lee, J. D., Moller, S. J., Lewis, A. C., Mendes, L., McQuaid, J. B., Oetjen, H., Saiz-Lopez, A., Pilling, M. J., and Plane, J. M. C.: Extensive halogen-mediated ozone destruction over the tropical Atlantic Ocean, Nature, 453, 7199, 1232-1235, 2008.

Rex, M., Wohltmann, I., Ridder, T., Lehmann, R., Rosenlof, K., Wennberg, P., Weisenstein, D., Notholt, J., Krüger, K., Mohr, V., and Tegtmeier, S.: A tropical West Pacific OH minimum and implications for stratospheric composition, Atmos. Chem. Phys., 14, 4827-4841, https://doi.org/10.5194/acp-14-4827-2014, 2014.

Saiz-Lopez, A., Lamarque, J.-F., Kinnison, D. E., Tilmes, S., Ordóñez, C., Orlando, J. J., Conley, A. J., Plane, J. M. C., Mahajan, A. S., Sousa Santos, G., Atlas, E. L., Blake, D. R., Sander, S. P., Schauffler, S., Thompson, A. M., and Brasseur, G.: Estimating the climate significance of halogen-driven ozone loss in the tropical marine troposphere, Atmos. Chem. Phys., 12, 3939-3949, https://doi.org/10.5194/acp-12-3939-2012, 2012.

Saiz-Lopez, A., Fernandez, R. P., Ordóñez, C., Kinnison, D. E., Gómez Martín, J. C., Lamarque, J.-F., and Tilmes, S.: Iodine chemistry in the troposphere and its effect on ozone, Atmos. Chem. Phys., 14, 13119-13143, https://doi.org/10.5194/acp-14-13119-2014, 2014.

Schultz, M.G., Schröder, S., Lyapina, O., Cooper, O., Galbally, I., Petropavlovskikh, I., von Schneidemesser, E., Tanimoto, H., Elshorbany, Y., Naja, M., Seguel, R., Dauert, U., Eckhardt, P., Feigenspahn, S., Fiebig, M., Hjellbrekke, A.-G., Hong, Y.-D., Christian Kjeld, P., Koide, H., Lear, G., Tarasick, D., Ueno, M., Wallasch, M., Baumgardner, D., Chuang, M.-T., Gillett, R., Lee, M., Molloy, S., Moolla, R., Wang, T., Sharps, K., Adame, J.A., Ancellet, G., Apadula, F., Artaxo, P., Barlasina, M., Bogucka, M., Bonasoni, P., Chang, L., Colomb, A., Cuevas, E., Cupeiro, M., Degorska, A., Ding, A., Fröhlich, M., Frolova, M., Gadhavi, H., Gheusi, F., Gilge, S., Gonzalez, M.Y., Gros, V., Hamad, S.H., Helmig, D., Henriques, D., Hermansen, O., Holla, R., Huber, J., Im, U., Jaffe, D.A., Komala, N., Kubistin, D., Lam, K.-S., Laurila, T., Lee, H., Levy, I., Mazzoleni, C., Mazzoleni, L., McClure-Begley, A., Mohamad, M., Murovic, M., Navarro-Comas, M., Nicodim, F., Parrish, D., Read, K.A., Reid, N., Ries, L., Saxena, P., Schwab, J.J., Scorgie, Y., Senik, I., Simmonds, P., Sinha, V., Skorokhod, A., Spain, G., Spangl, W., Spoor, R., Springston, S.R., Steer, K., Steinbacher, M., Suharguniyawan, E., Torre, P., Trickl, T., Weili, L., Weller, R., Xu, X., Xue, L. and Zhiqiang, M.: Tropospheric Ozone Assessment Report: Database and metrics data of global surface ozone observations. Elem Sci Anth., 5, p58. DOI: http://doi.org/10.1525/elementa.244, 2017.

Sekiya, T., Miyazaki, K., Ogochi, K., Sudo, K., and Takigawa, M.: Global high-resolution simulations of tropospheric nitrogen dioxide using CHASER V4.0, Geosci. Model Dev., 11, 959-988, https://doi.org/10.5194/gmd-11-959-2018, 2018.

Sherwen, T., Evans, M. J., Carpenter, L. J., Andrews, S. J., Lidster, R. T., Dix, B., Koenig, T. K., Sinreich, R., Ortega, I., Volkamer, R., Saiz-Lopez, A., Prados-Roman, C., Mahajan, A. S., and Ordóñez, C.: Iodine's impact on tropospheric oxidants: a global model study in GEOS-Chem, Atmos. Chem. Phys., 16, 1161-1186, https://doi.org/10.5194/acp-16-1161-2016, 2016.

Shindell, D., Zeng, G., Lamarque, J. F., Szopa, S., Nagashima, T., Naik, V., Eyring, V., and Collins, W.: The model data outputs from the Atmospheric Chemistry & Climate Model Intercomparison Project (ACCMIP), NCAS British Atmospheric Data Centre, date of citation: 17 Apr 2019, http://catalogue.ceda.ac.uk/uuid/ded523bf23d59910e5d73f1703a2d540, 2011.

Singh, H. B., Gregory, G. L., Anderson, B., Browell, E., Sachse, G. W., Davis, D. D., Crawford, J., Bradshaw, J. D., Talbot, R., Blake, D. R., Thornton, D., Newell, R., and Merrill, J.: Low ozone in the marine boundary layer of the tropical Pacific Ocean: Photochemical loss, chlorine atoms, and entrainment, J. Geophys. Res., 101(D1), 1907–1917, doi: 10.1029/95JD01028, 1996.

Stevenson, D. S., Young, P. J., Naik, V., Lamarque, J.-F., Shindell, D. T., Voulgarakis, A., Skeie, R. B., Dalsoren, S. B., Myhre, G., Berntsen, T. K., Folberth, G. A., Rumbold, S. T., Collins, W. J., MacKenzie, I. A., Doherty, R. M., Zeng, G., van Noije, T. P. C., Strunk, A., Bergmann, D., Cameron-Smith, P., Plummer, D. A., Strode, S. A., Horowitz, L., Lee, Y. H., Szopa, S., Sudo, K., Nagashima, T., Josse, B., Cionni, I., Righi, M., Eyring, V., Conley, A., Bowman, K. W., Wild, O., and Archibald, A.: Tropospheric ozone changes, radiative forcing and attribution to emissions in the Atmospheric Chemistry and Climate Model Intercomparison Project (ACCMIP), Atmos. Chem. Phys., 13, 3063–3085, https://doi.org/10.5194/acp-13-3063-2013, 2013.

Sudo, K., Takahashi, M., J.-I. Kurokawa, and Akimoto, H.: CHASER: A global chemical model of the troposphere 1. Model description, J. Geophys. Res., 107(D17), 4339, doi:10.1029/2001JD001113, 2002.

Takashima, H., Shiotani, M., Fujiwara, M., Nishi, N., Hasebe, F.: Ozonesonde observations at Christmas Island (2°N, 157°W) in the equatorial central Pacific. J. Geophys. Res. 113, D10112, doi:10.1029/2007JD009374, 2008.

Takashima, H., Kanaya, Y., and Taketani, F.: Downsizing of a ship-borne MAX-DOAS instrument, JAMSTEC Rep. Res. Dev., 23, 34-40, 2016. (Japanese with English abstract)

Taketani, F., Miyakawa, T., Takashima, H., Komazaki, Y., Pan, X., Kanaya, Y., and Inoue, J.: Shipborne observations of atmospheric black carbon aerosol particles over the Arctic Ocean, Bering Sea, and North Pacific Ocean during September 2014, J. Geophys. Res. Atmos., 121, 1914–1921, doi: 10.1002/2015JD023648, 2016.

Tanimoto, H., Matsumoto, K., and Uematsu, M.: Ozone-CO Correlations in Siberian Wildfire Plumes Observed at Rishiri Island, SOLA, 4,65-68, 2008.

Thompson, A. M., Witte, J. C., Sterling, C., Jordan, A., Johnson, B. J., Oltmans, S. J., Fujiwara, M., Vömel, H., Allaart, M., Piters, A., Coetzee, G. J. R., Posny, F., Corrales, E., Diaz, J. A., Félix, C., Komla, N., Lai, N., Ahn Nguyen, H. T., Maata, M., Mani, F., Zainal, Z., Ogino, S.-Y., Paredes, F., Bezerra Penha, T. L., da Silva, F. R., Sallons-Mitro, S., Selkirk, H. B., Schmidlin, F. J., Stübi, R., and Thiongo, K.: First reprocessing of Southern Hemisphere Additional Ozonesondes (SHADOZ) ozone profiles (1998-2016): 2. Comparisons with satellites and ground-based instruments. Journal of Geophysical Research: Atmospheres, 122, 13,000-13,025. https://doi.org/10.1002/2017JD027406, 2017.

Tilmes, S., Lamarque, J.-F., Emmons, L. K., Kinnison, D. E., Marsh, D., Garcia, R. R., Smith, A. K., Neely, R. R., Conley, A., Vitt, F., Val Martin, M., Tanimoto, H., Simpson, I., Blake, D. R., and Blake, N.: Representation of the Community Earth System Model (CESM1) CAM4-chem within the Chemistry-Climate Model Initiative (CCMI), Geosci. Model Dev., 9, 1853-1890, https://doi.org/10.5194/gmd-9-1853-2016, 2016.

Watanabe, K., Nojiri, Y., and Kariya, S.: Measurements of ozone concentrations on a commercial vessel in the marine boundary layer over the northern North Pacific Ocean, J. Geophys. Res., 110, D11310, doi: 10.1029/2004JD005514, 2005.

Weiss-Penzias, P., Jaffe, D. A., Swartzendruber, P., Dennison, J. B., Chand, D., Hafner, W., and Prestbo, E.: Observations of Asian air pollution in the free troposphere at Mount Bachelor Observatory during the spring 2004, J. Geophys. Res., 111, D10304, doi:10.1029/2005JD006522, 2006.

Wesely, M. L.: Parameterization of surface resistance to gaseous dry deposition in regional-scale numerical models, Atmos. Environ., 23, 1293-1304, 1989.

Wofsy, S. C., HIPPO science team, cooperating modellers and satellite teams, HIAPER Pole-to-Pole Observations (HIPPO): fine-grained, global-scale measurements of climatically important atmospheric gases and aerosols, Phil. Trans. R. Soc. A, 369, 2073-2086, doi:10.1098/rsta.2010.0313, 2011.

Young, P. J., Naik, V., Fiore, A. M., Gaudel, A., Guo, J., Lin, M. Y., Neu, J. L., Parrish, D. D., Rieder, H. E., Schnell, J. L., Tilmes, S., Wild, O., Zhang, L., Ziemke, J. R., Brandt, J., Delcloo, A., Doherty, R. M., Geels, C., Hegglin, M. I., Hu, L., Im, U., Kumar, R., Luhar, A., Murray, L., Plummer, D., Rodriguez, J., Saiz-Lopez, A., Schultz, M.G., Woodhouse, M. T. and Zeng, G.: Tropospheric Ozone Assessment Report: Assessment of global-scale model performance for global and regional ozone distributions, variability, and trends, Elem Sci Anth., 6(1), p.10. DOI: http://doi.org/10.1525/elementa.265, 2018.

Young, P. J., Archibald, A. T., Bowman, K. W., Lamarque, J.-F., Naik, V., Stevenson, D. S., Tilmes, S., Voulgarakis, A., Wild, O., Bergmann, D., Cameron-Smith, P., Cionni, I., Collins,W. J., Dalsøren, S. B., Doherty, R. M., Eyring, V., Faluvegi, G., Horowitz, L. W., Josse, B., Lee, Y. H., MacKenzie, I. A., Nagashima, T., Plummer, D. A., Righi, M., Rumbold, S. T., Skeie, R. B., Shindell, D. T., Strode, S. A., Sudo, K., Szopa, S., and Zeng, G.: Preindustrial to end 21st century projections of tropospheric ozone from the Atmospheric Chemistry and Climate Model Intercomparison Project (ACCMIP), Atmos. Chem. Phys., 13, 2063– 2090, https://doi.org/10.5194/acp-13-2063-2013, 2013.

Zhang, B., Owen, R. C., Perlinger, J. A., Helmig, D., Val Martín, M., Kramer, L., Mazzoleni, L. R. and Mazzoleni, C.: Ten-year chemical signatures associated with long-range transport observed in the free troposphere over the central North Atlantic, Elem Sci Anth, 5, p.8, DOI: https://doi.org/10.1525/elementa.194, 2017.

Zhu, C., Kanaya, Y., Yoshikawa-Inoue, H., Irino, T., Seki, O., and Tohjima, Y.: Sources of atmospheric black carbon and related carbonaceous components at Rishiri Island, Japan: The roles of Siberian wildfires and of crop residue burning in China, Environmental Pollution, 247, 55-63, doi:10.1016/j.envpol.2019.01.003, 2019.

Table 1. Overview of cruise legs of R/V *Mirai* used in this study.

Cruise	Study area	Departure		Arrival		Remark
MR12-02 Leg1	Western North Pacific	00:00UTC 4 Jun 2012	Mutsu	08:00UTC 24 Jun 2012	Onahama (out of port)	
MR12-02 Leg2	Western North Pacific	08:00UTC 24 Jun 2012	Onahama (out of port)	00:00UTC 12 Jul 2012	Mutsu	Hachinohe Port from 0030 to 0800 UTC Jul 11 (no data)
MR13-04	Western North Pacific	23:50UTC 9 Jul 2013	Yokohama	00:00UTC 29 Jul 2013	Mutsu	
MR13-05	Bering Sea	23:50UTC 12 Aug 2013	Mutsu	17:40UTC 26 Aug 2013	Dutch Harbor	
MR13-06 Leg1	Arctic Ocean, Bering Sea	18:00UTC 28 Aug 2013	Dutch Harbor	18:40UTC 7 Oct 2013	Dutch Harbor	
MR13-06 Leg2	Bering Sea, North Pacific	17:40UTC 9 Oct 2013	Dutch Harbor	23:50UTC 20 Oct 2013	Mutsu	
MR14-01	East Indian Ocean, Equatorial Region	23:00UTC 8 Jan 2014	Mutsu	00:00UTC 13 Feb 2014	Palau	
MR14-02	Western Pacific, Equatorial Region	00:00UTC 15 Feb 2014	Koror, Palau	00:00UTC 23 Mar 2014	Mutsu	Hachinohe Port, 0400-0900UTC 21 Mar 2014 (no data)
MR14-04 Leg1	Western North Pacific	22:10UTC 8 Jul 2014	Yokohama	04:00UTC 15 Jul 2014	Kushiro	
MR14-04 Leg2	North Pacific	01:00UTC 17 Jul 2014	Kushiro	17:50UTC 29 Aug 2014	Dutch Harbor	
MR14-05	Arctic Ocean, Bering Sea, North Pacific	18:10UTC 31 Aug 2014	Dutch Harbor	00:20UTC 10 Oct 2014	Yokohama	
MR14-06 Leg1	Western Pacific, Equatorial region	06:10UTC 4 Nov 2014	Mutsu	23:20UTC 17 Dec 2014	Chuuk	Yokohama Port, from 2310UTC 5 Nov to 0700UTC 7 Nov (with data)
MR14-06 Leg2	Western Pacific Equatorial region	00:07UTC 20 Dec 2014	Chuuk	00:10UTC 19 Jan 2015	Palau	
MR14-06 Leg3	Western Pacific, East Indian Ocean Equatorial Region	00:00UTC 22 Jan 2015	Palau	00:00UTC 25 Feb 2015	Mutsu	Hachinohe Port, from 2330UTC 23 Feb to 0700UTC 24 Feb (with data)
MR15-03 leg 1	North Pacific, Bering Sea, Arctic Ocean	22:50UTC 23 Aug 2015	Mutsu	18:50UTC 6 Oct 2015	Dutch Harbor	
MR15-03 leg 2	Bering Sea, North Pacific	18:10UTC 9 Oct 2015	Dutch Harbor	23:50UTC 21 Oct 2015	Mutsu	Hachinohe Port, from 2300UTC 20 Oct to 0650UTC 21 Oct (with data)
MR15-04	Western Pacific, East Indian Ocean Equatorial Region	06:00UTC 5 Nov 2015	Mutsu	02:20UTC 20 Dec 2015	Jakarta	Hachinohe Port, from 2250UTC 5 Nov to 0620UTC 6 Nov (with data)
MR15-05 leg 1	East Indian Ocean	03:10UTC 23 Dec 2015	Jakarta	00:50UTC 11 Jan 2016	Bali	
MR15-05 leg 2	East Indian	01:00UTC	Benoa, Bali	23:50UTC	Yokohama	

	Ocean, Western North Pacific	13 Jan 2016		24 Jan 2016		
MR16-06	Arctic Ocean, Bering Sea, North Pacific	00:00UTC 22 Aug 2016	Hachinohe	00:00UTC 5 Oct 2016	Mutsu	Nome port, 1600-2010UTC 23 Sep (with data); Hachinohe Port from 2230UTC 3 Oct to 0720UTC 4 Oct (with data)
MR16-08	Western Pacific Equatorial Region	07:00UTC 27 Nov 2016	Shimizu	21:00UTC 23 Dec 2016	Suva	
MR16-09 leg 1	South Pacific	17:10UTC 26 Dec 2016	Suva	11:00UTC 17 Jan 2017	Puerto Mont	
MR16-09 leg 3	Southern Ocean	13:10UTC 8 Feb 2017	Punta Arenas	21:00UTC 4 Mar 2017	Auckland	
MR16-09 leg 4	Western Pacific	21:20UTC 7 Mar 2017	Auckland	00:00UTC 28 Mar 2017	Mutsu	Hachinohe Port, from 2240UTC 26 Mar to 0650UTC 27 Mar (with data)

Table 2. Cases of long-range transport events used for examination of photochemistry (unit for $\Delta O_3/\Delta CO$ is ppbv/ppbv).

case	Start time	End time	Latitude (°N)	Longitude (°E)	R (obs)	$\Delta O_3/\Delta CO$ (obs)	R (TCR-2)	$\Delta O_3/\Delta CO$ (TCR-2)	COmax (obs)	COmax (TCR-2)	O_3max (obs)	O_3max (TCR-2)
A	22:00UTC 15 Aug 2013	22:00UTC 17 Aug 2013	41.32–45.22	151.81–162.71	0.81	0.42±0.04	0.68	0.96±0.15	101.6	87.5	38.2	40.0
B	12:00UTC 23 Aug 2013	12:00UTC 25 Aug 2013	54.47–56.59	182.07–193.25	0.79	0.28±0.03	-0.30	-0.12±0.06	101.9	102.7	33.1	26.0
C	00:00 UTC 05 Oct 2013	22:00 UTC 06 Oct 2013	56.95–65.12	191.36–192.82	0.80	0.54±0.06	0.85	0.86±0.08	116.4	117.2	43.1	38.7
D	23:00 UTC 16 Oct 2013	23:00 UTC 18 Oct 2013	40.08–40.88	143.72–154.34	0.75	0.32±0.04	0.58	0.15±0.03	137.4	129.2	51.1	40.9
E	15:00 UTC 12 Jan 2014	15:00 UTC 14 Jan 2014	25.21–31.33	126.85–136.28	0.66	0.03±0.01	0.29	0.01±0.01	331.2	269.7	52.8	45.8
F	00:00 UTC 13 Mar 2014	00:00 UTC 15 Mar 2014	11.51–18.95	151.64–154.58	0.83	0.34±0.03	0.93	0.51±0.03	137.4	125.3	35.4	37.3
G	00:00 UTC 17 Mar 2014	00:00 UTC 19 Mar 2014	25.08–34.12	145.21–149.15	0.86	0.11±0.01	0.75	0.06±0.01	299.1	219.0	66.6	56.3
H	13:00 UTC 24 Jul 2014	10:00 UTC 26 Jul 2014	42.67–45.32	152.68–157.02	0.57	0.38±0.09	0.92	0.23±0.01	132.2	208.0	48.2	47.9
I	00:00 UTC 02 Aug 2014	00:00 UTC 04 Aug 2014	46.99–47.01	171.62–177.97	0.90	0.11±0.01	0.93	0.14±0.01	249.4	220.0	38.0	37.2
J	00:00 UTC 25 Aug 2014	00:00 UTC 27 Aug 2014	51.15–53.38	208.00–221.14	0.87	0.53±0.04	0.70	0.15±0.02	119.0	116.1	35.4	31.5
K	00:00 UTC 08 Nov 2014	00:00 UTC 10 Nov 2014	26.61–32.60	141.81–149.90	0.92	0.44±0.03	0.67	0.23±0.04	154.4	145.1	55.6	46.4
L	02:00 UTC 07 Feb 2015	21:00 UTC 08 Feb 2015	-1.60–2.16	89.95–90.19	0.95	0.21±0.01	0.96	0.60±0.03	181.1	105.7	31.8	24.4
M	00:00 UTC 18 Feb 2015	00:00 UTC 20 Feb 2015	24.42–30.05	123.50–131.79	0.86	0.05±0.004	0.19	0.02±0.02	390.7	222.1	58.9	51.5
N	17:00 UTC 21 Feb 2015	17:00 UTC 23 Feb 2015	34.29–40.27	139.89–142.33	-0.27	-0.03±0.02	-0.20	-0.04±0.03	478.6	220.6	53.6	52.9
O	00:00 UTC 05 Oct 2015	17:00 UTC 06 Oct 2015	53.98–60.57	192.01–193.51	0.76	0.38±0.05	0.38	0.09±0.03	127.3	126.2	46.1	36.1
P	14:00 UTC 16 Nov 2015	12:00 UTC 18 Nov 2015	-9.21–-0.19	114.13–119.13	0.82	0.29±0.03	0.83	0.37±0.04	148.8	185.0	28.9	48.7
Q	18:00 UTC 16 Dec 2015	15:00 UTC 18 Dec 2015	-6.14–-4.04	101.01–102.27	0.39	0.09±0.04	-0.75	-0.03±0.005	94.7	214.4	18.8	17.5
R	04:00 UTC 27 Dec 2015	04:00 UTC 29 Dec 2015	-24.78–-21.16	110.59–112.77	0.90	0.33±0.03	0.89	0.44±0.03	82.7	93.1	28.3	37.3
S	08:00 UTC 23 Jan 2016	20:00 UTC 24 Jan 2016	31.97–35.03	138.91–139.94	-0.40	-0.02±0.01	-0.63	-0.21±0.05	357.8	168.5	46.4	46.3
T	01:00 UTC 25 Sep 2016	01:00 UTC 27 Sep 2016	54.78–61.49	173.23–184.47	-0.74	-0.03±0.004	-0.74	-0.16±0.02	555.7	161.4	47.9	45.3
U	12:00 UTC 27 Sep 2016	12:00 UTC 29 Sep 2016	47.42–53.85	161.78–171.57	0.00	0.00±0.01	-0.78	-0.10±0.01	317.9	139.6	43.6	36.1
V	12:00 UTC 03 Dec 2016	10:00 UTC 05 Dec 2016	7.66–12.46	136.43–137.00	0.67	0.24±0.04	0.97	0.60±0.03	92.7	99.1	25.1	34.8
W	00:00 UTC 20 Mar 2017	00:00 UTC 22 Mar 2017	19.86–27.70	147.83–152.62	0.81	0.25±0.03	0.83	0.13±0.02	214.8	214.6	63.0	59.0

Figure 1. continued.
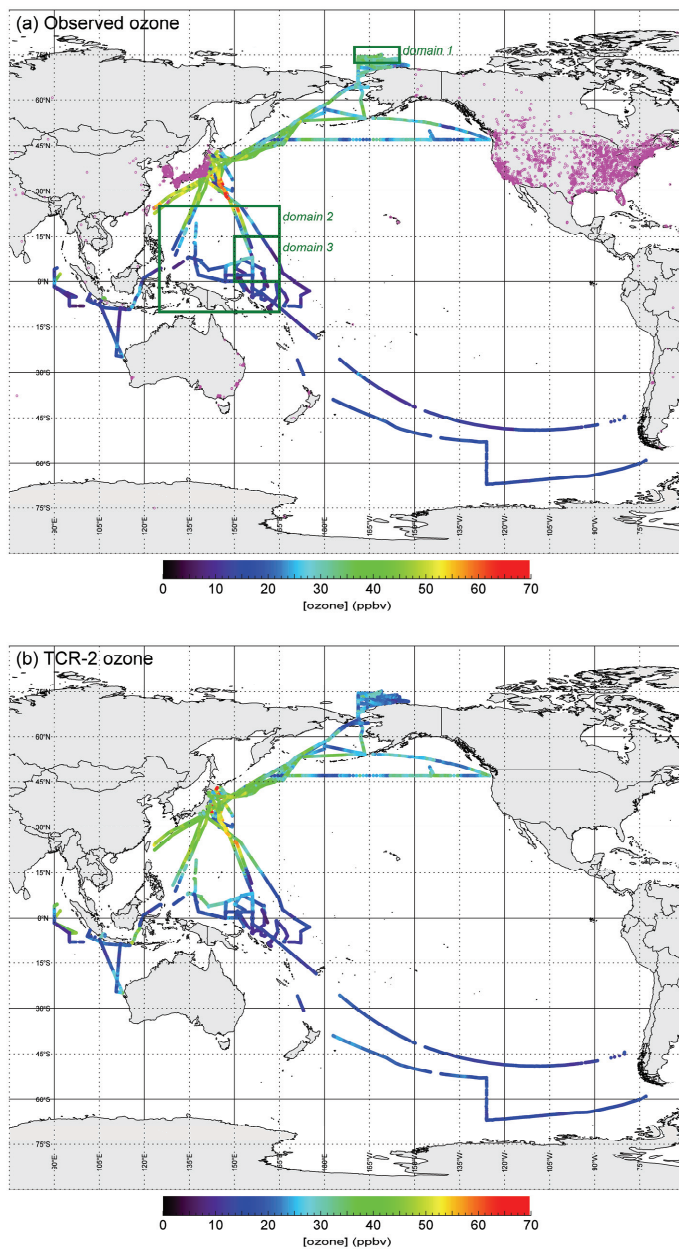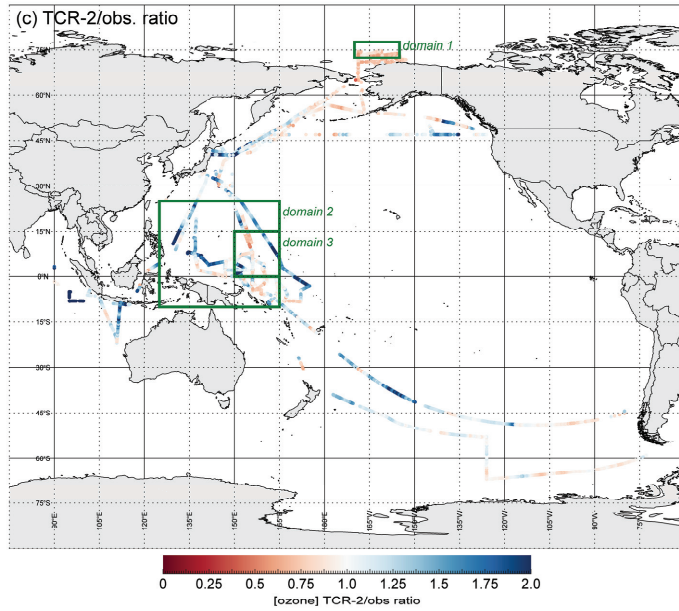
Figure 1. Geographical distributions from (a) observed hourly O$_3$ mixing ratios (N = 11 666) on R/V *Mirai* during 24 research cruise legs in 2012–2017 and (b) those from reanalysis (TCR-2) of data along R/V *Mirai* cruise track; (c) reanalysis/observation ratios (TCR-2/obs) for O$_3$ mixing ratios. In (a) stationary points of TOAR data set are plotted (magenta dots). In (a) and (c), three green rectangles show focused domains in Arctic (domain 1, 72.5–77.5° N, 190–205° E) and two in western Pacific equatorial region (domain 2, 10° S to 25° N, 125–165° E; domain 3, 0–15° N, 150–165° E).
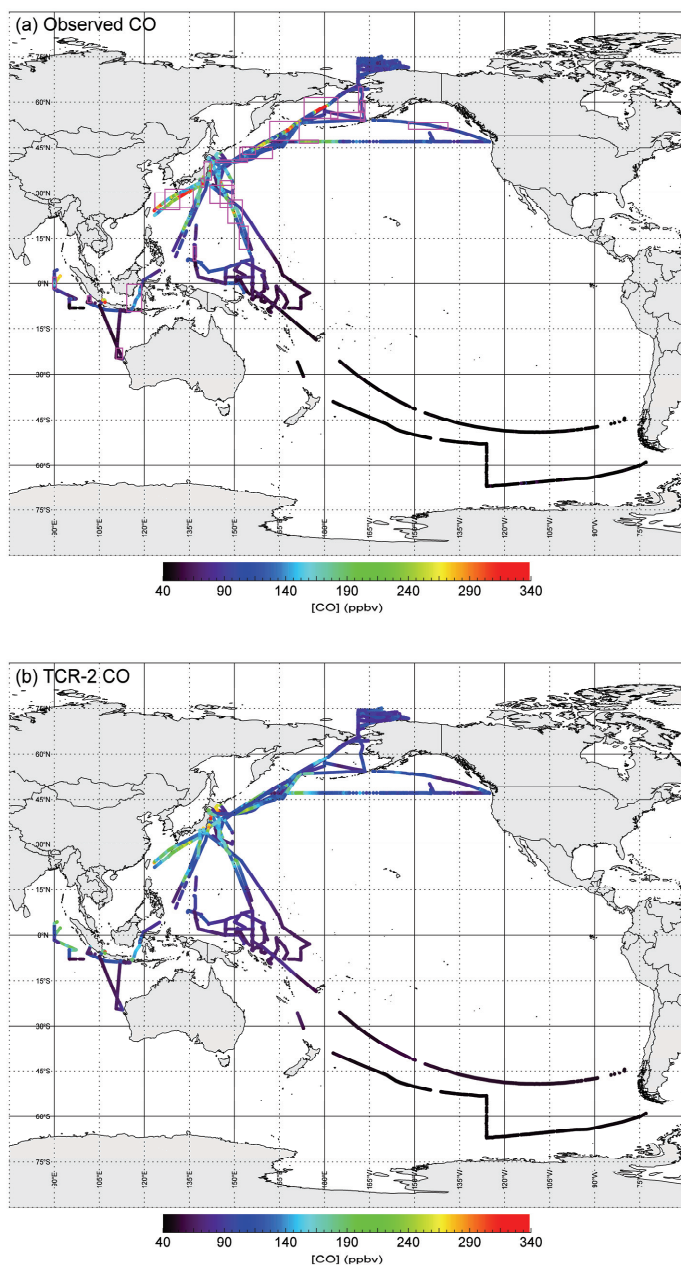
Figure 2. Geographical distributions of (a) observed CO mixing ratios and (b) those from TCR-2. In (a) magenta boxes indicate 23 regions where $\Delta O_3/\Delta CO$ ratios were analyzed (see Fig. 8 and Table 2).
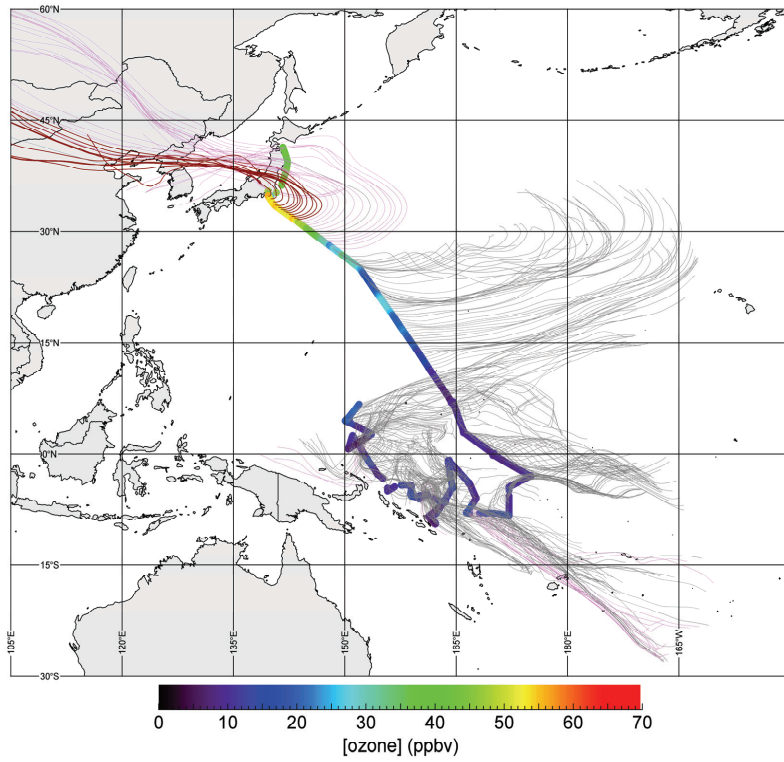
Figure 3. Observed O$_3$ mixing ratios during MR14-06 Leg 1 and backward trajectories (120 h). Magenta lines indicate cases in which trajectory entered regions over land (at altitudes < 2500 m a.s.l.). Red lines indicate cases in which observed O$_3$ mixing ratios exceeded 50 ppbv.
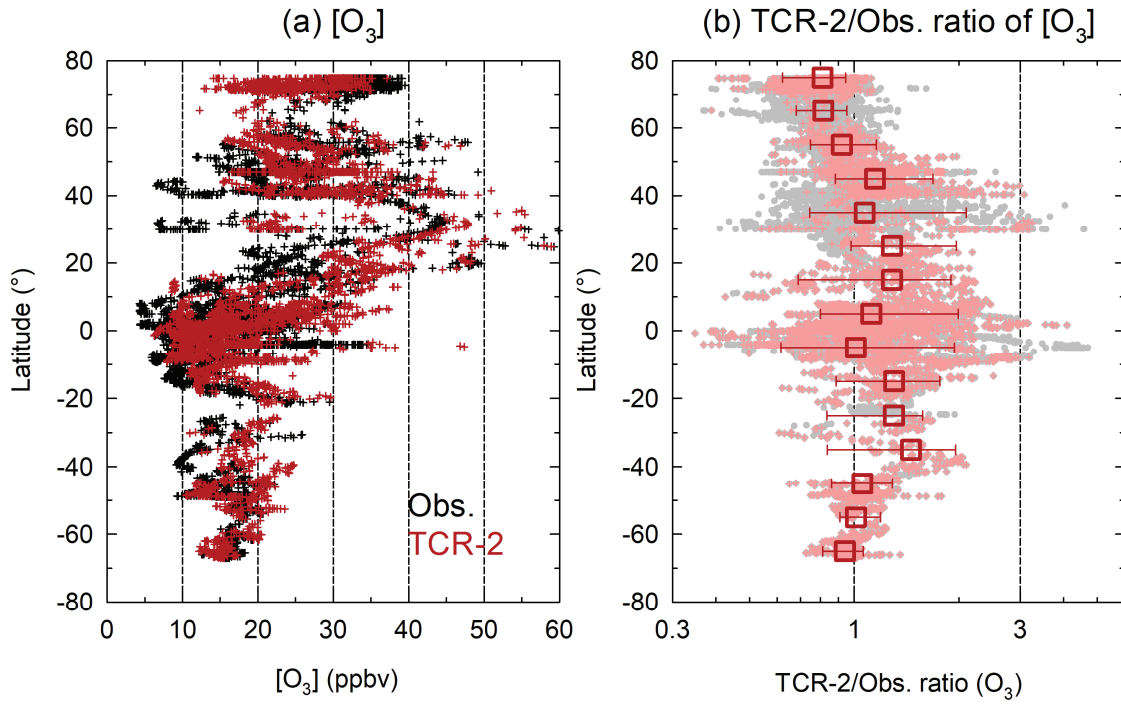
Figure 4. (a) Latitudinal distribution of O_3 mixing ratios from observation (black) and TCR-2 (red). Data are limited to cases of marine origins where difference between predicted and observed CO mixing ratios was less than 50 ppbv ($N = 5647$). (b) Latitudinal distribution of TCR-2/observation ratio for O_3 (light red dots) and binned medians (ranges are from 10th to 90th percentile) over 10°. Gray dots represent all cases without data selection.
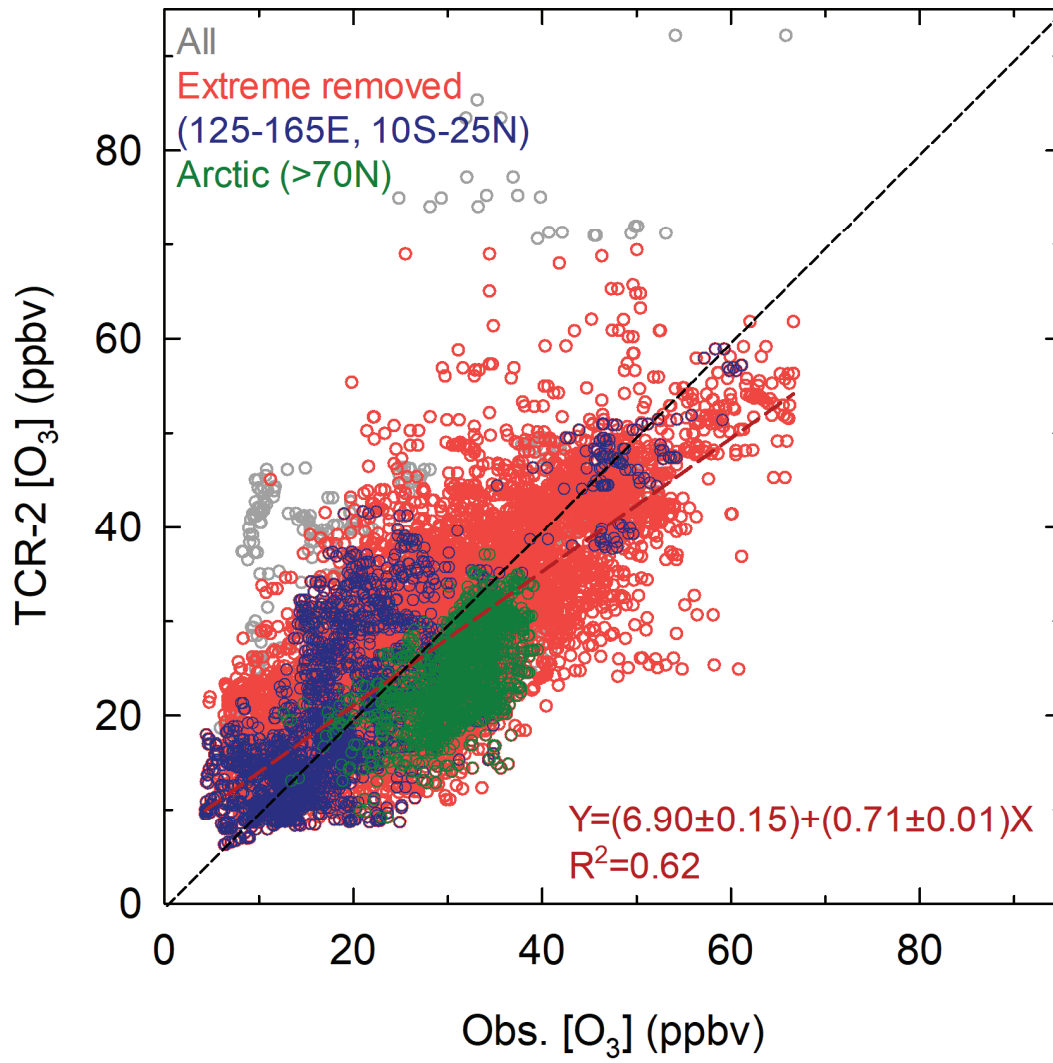
Figure 5. Scatterplot of observed and reanalysis O_3 mixing ratios. Gray circles include all data ($N = 11\,666$), red circles are cases when data from MR14-01 and extreme cases when TCR-2 exceeded 70 ppbv were removed. Green circles indicate data from Arctic region (>70° N) and blue circles indicate data from domain 2 (125–165° E, 10° S to 25° N).
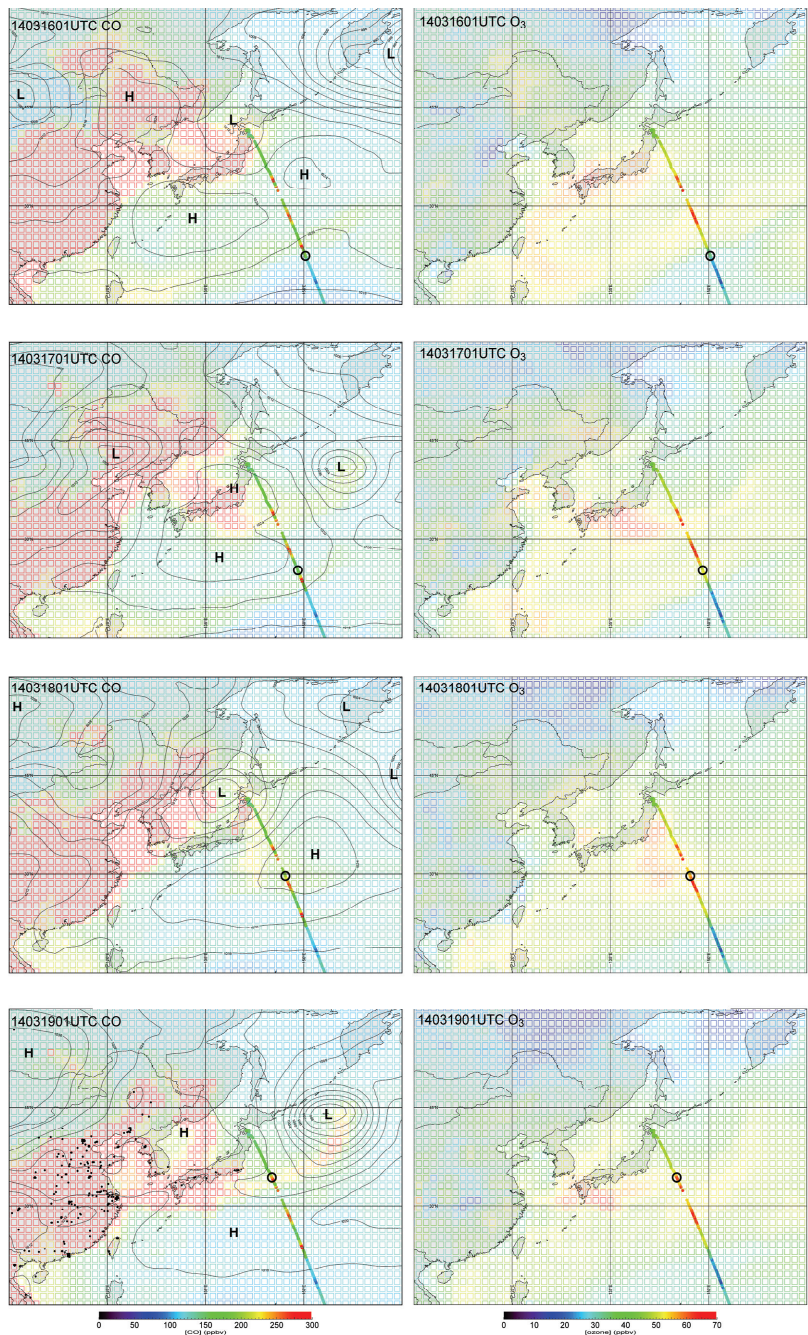
Figure 6. Temporal evolution of surface CO and O_3 distribution from TCR-2 (colored open squares) and from observations on R/V *Mirai* (all data, position of vessel is black circle) during MR14-02. Black circles in 14031901UTC CO panel indicate locations with high anthropogenic CO emissions (EDGAR).
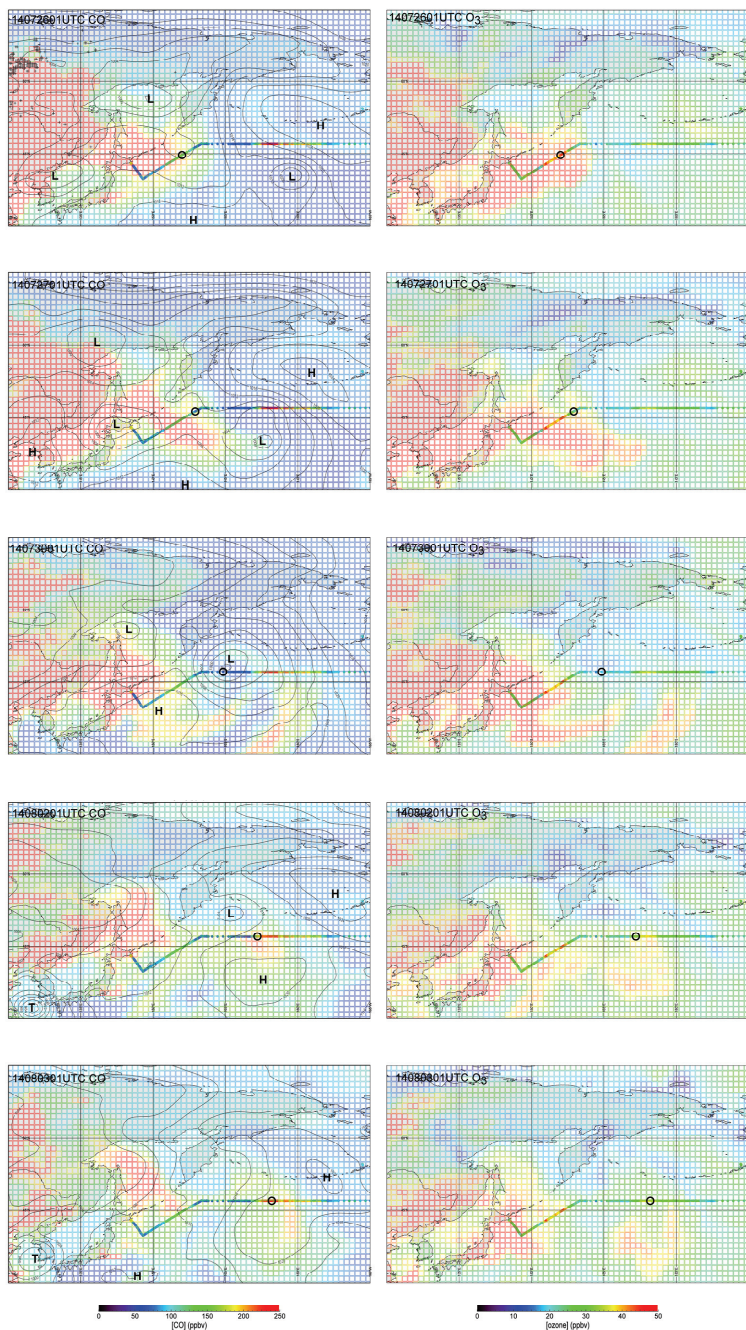
Figure 7. Temporal evolution of surface CO and O₃ distribution from TCR-2 (colored open squares) and from observations on R/V *Mirai* (all data, position of vessel is shown by black circle) during MR14-04 Leg 2. Plus signs in top-left panel show points with high carbon emissions from wildfires (GFED).
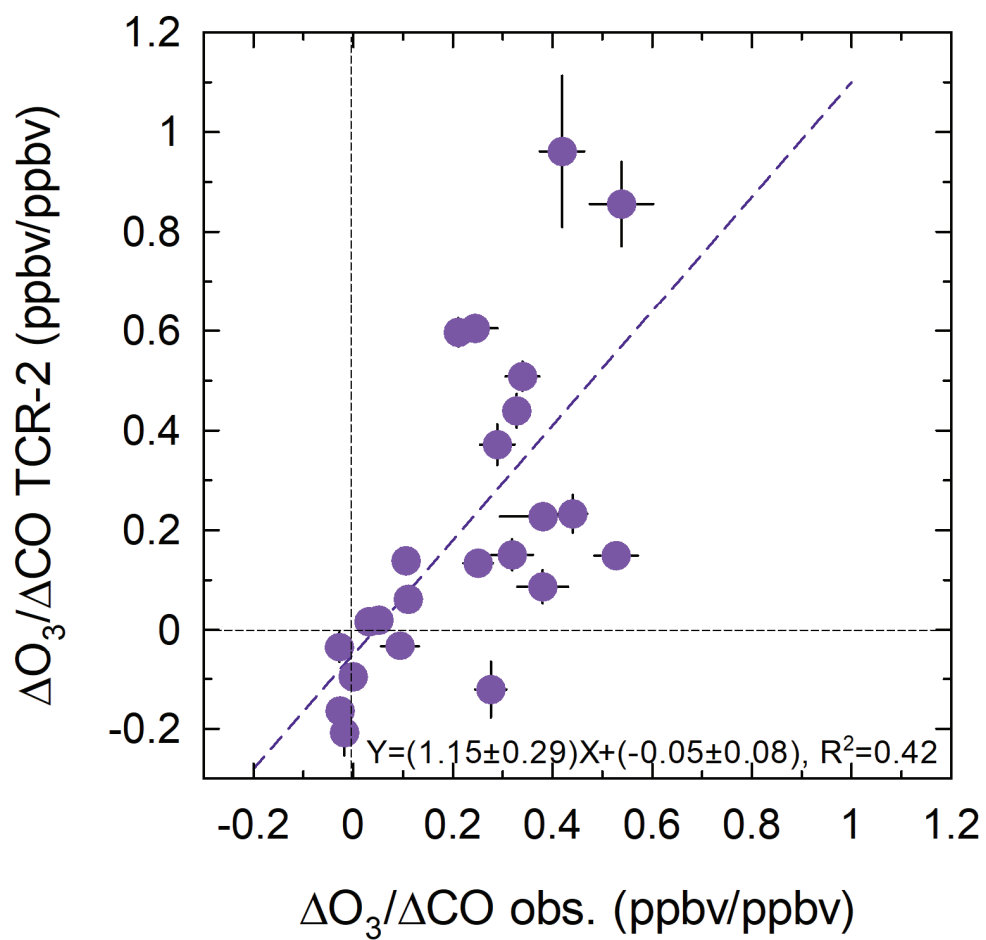
Figure 8. Correlations between $\Delta O_3/\Delta CO$ ratios from observations and TCR-2.
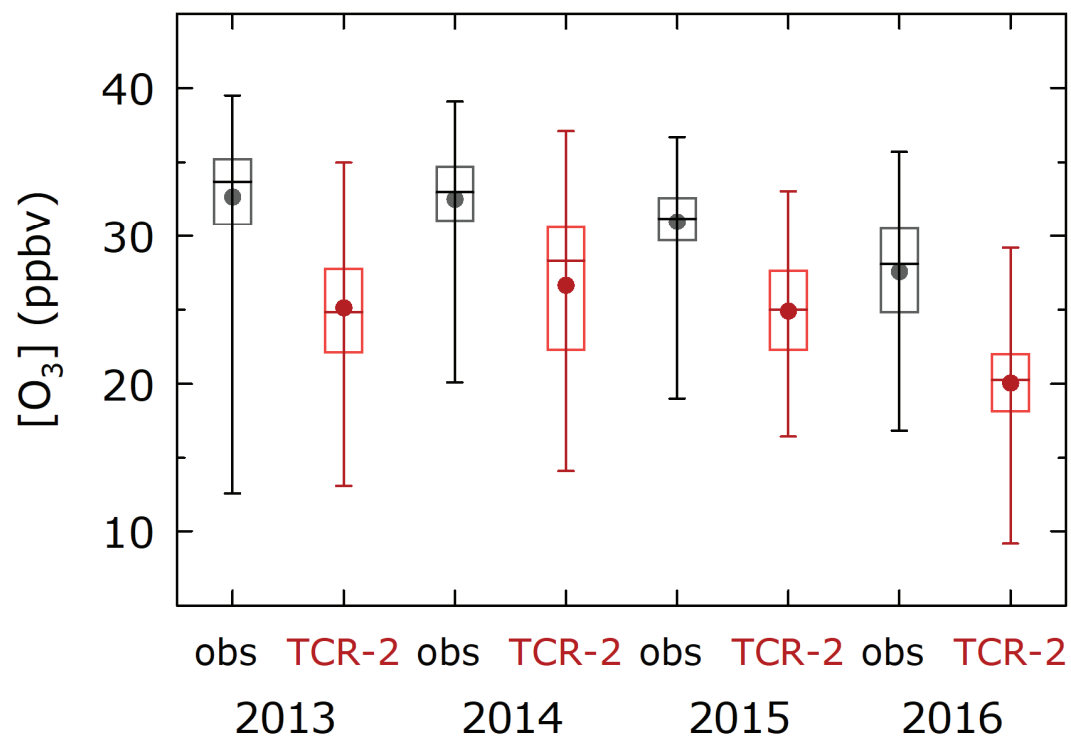
Figure 9. Repeated underestimations of O$_3$ mixing ratios ranges by TCR-2 relative to observed values in Arctic region (>70° N). Boxes and horizontal bars indicate 75 %, 50 % (median), and 25 %, and whiskers indicate 90 % and 10 %. Circles are averages.
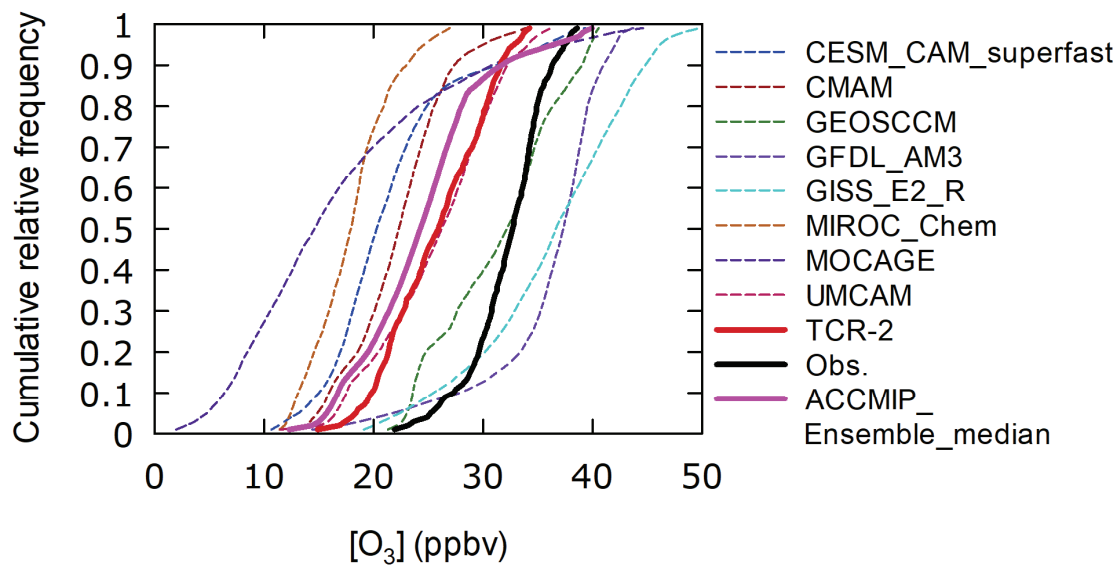
Figure 10. Cumulative relative frequency distributions of O₃ mixing ratios from observations (black), TCR-2 (red), and
members and ensemble median of ACCMIP in Arctic grid 1 [72.5–77.5° N and 190–205° E (155–170° W)] in September.
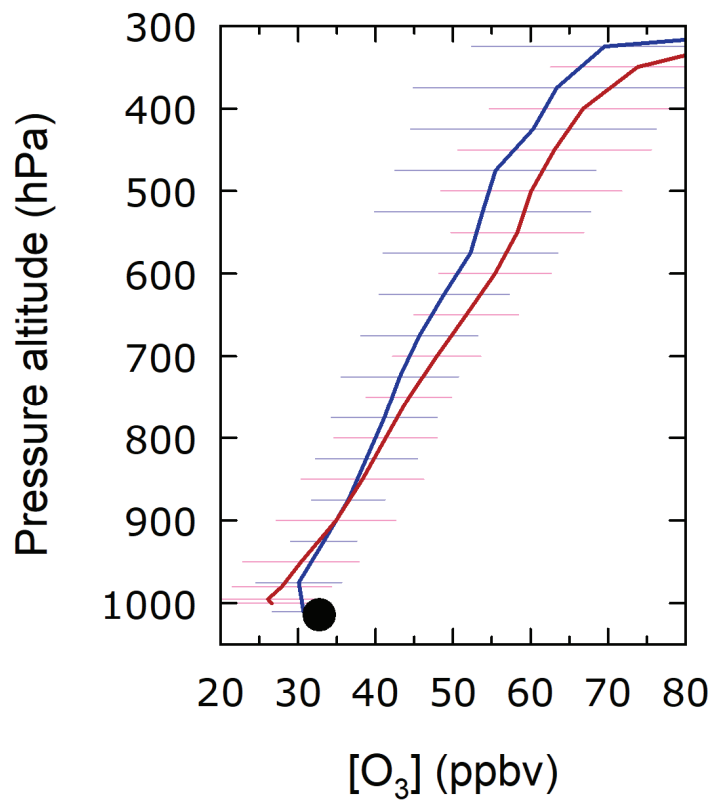
Figure 11. Average profile from O₃ soundings (blue) and that from TCR-2 (red). Average from surface observations on R/V *Mirai* is shown as black circle.
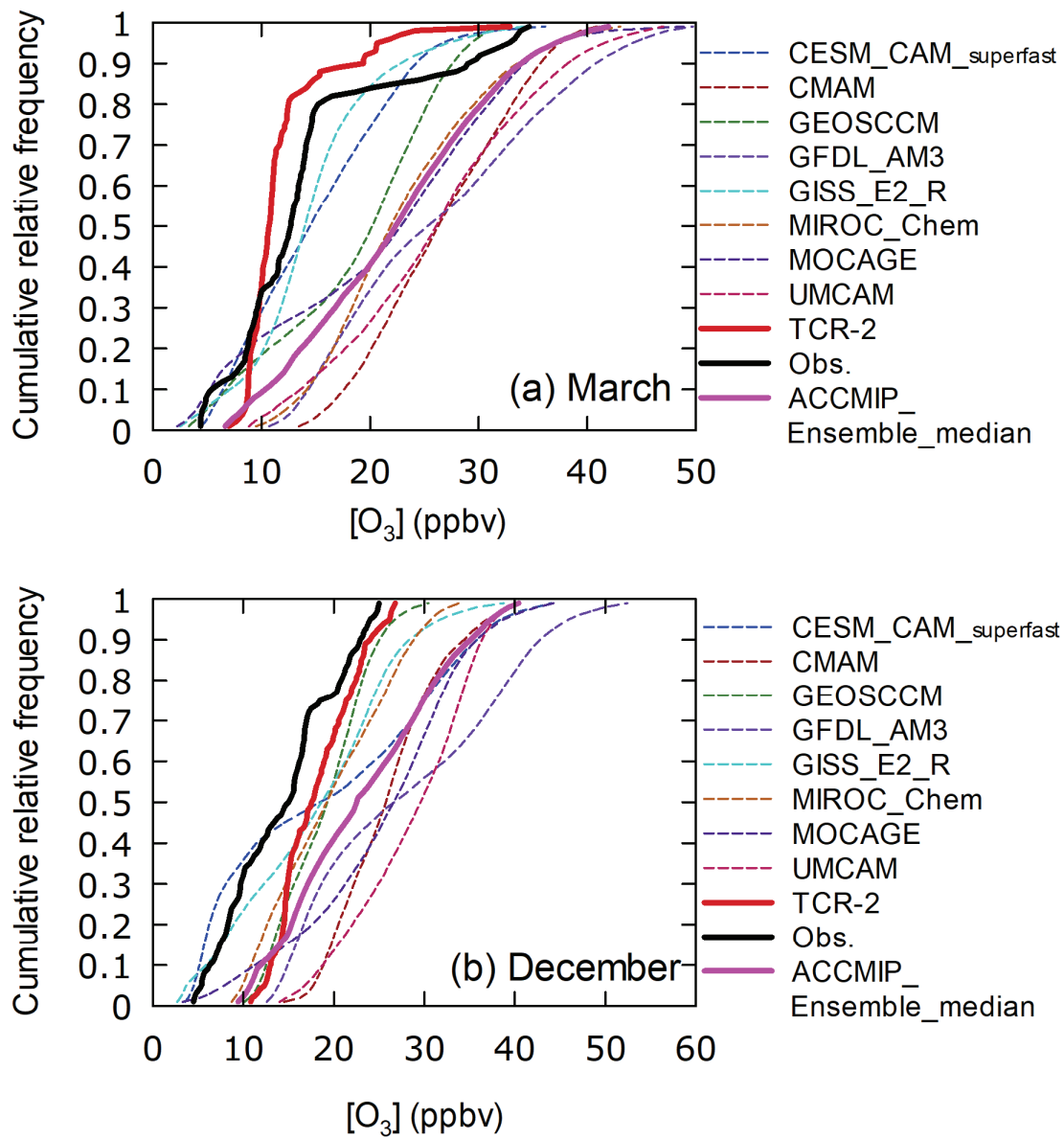
Figure 12. Cumulative relative frequency distributions of O_3 mixing ratios from observations (black), TCR-2 (red), and members and ensemble median of ACCMIP for domain 3 (0–15° N and 150–165° E) in (a) March and (b) December.
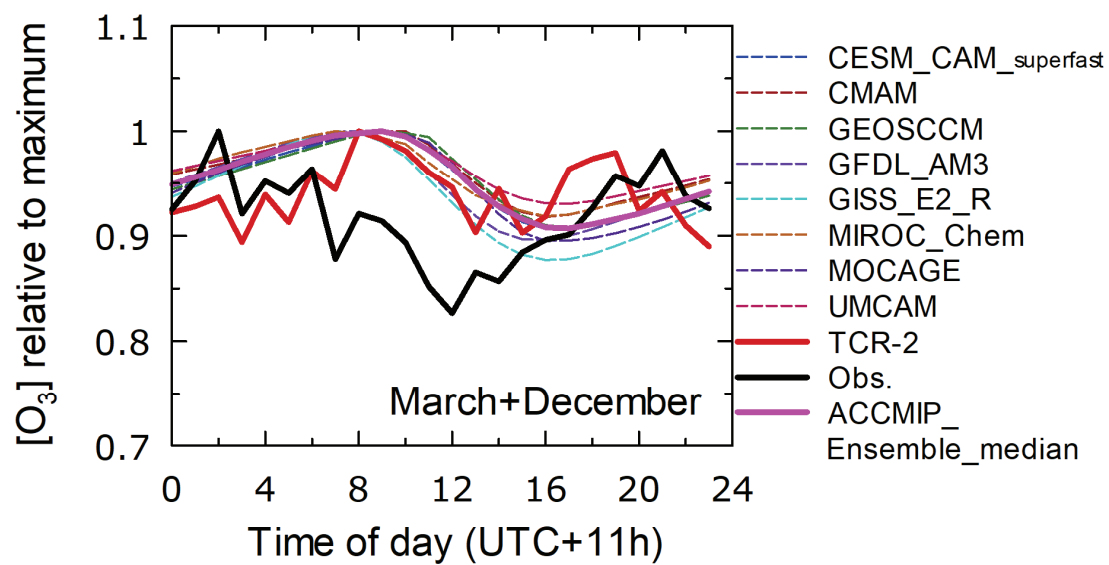
Figure 13. Diurnal variation patterns relative to maximum mixing ratios from observations (black), TCR-2 (red), and members and ensemble median of ACCMIP for domain 3 (0–15° N and 150–165° E). Data from March and December are merged.
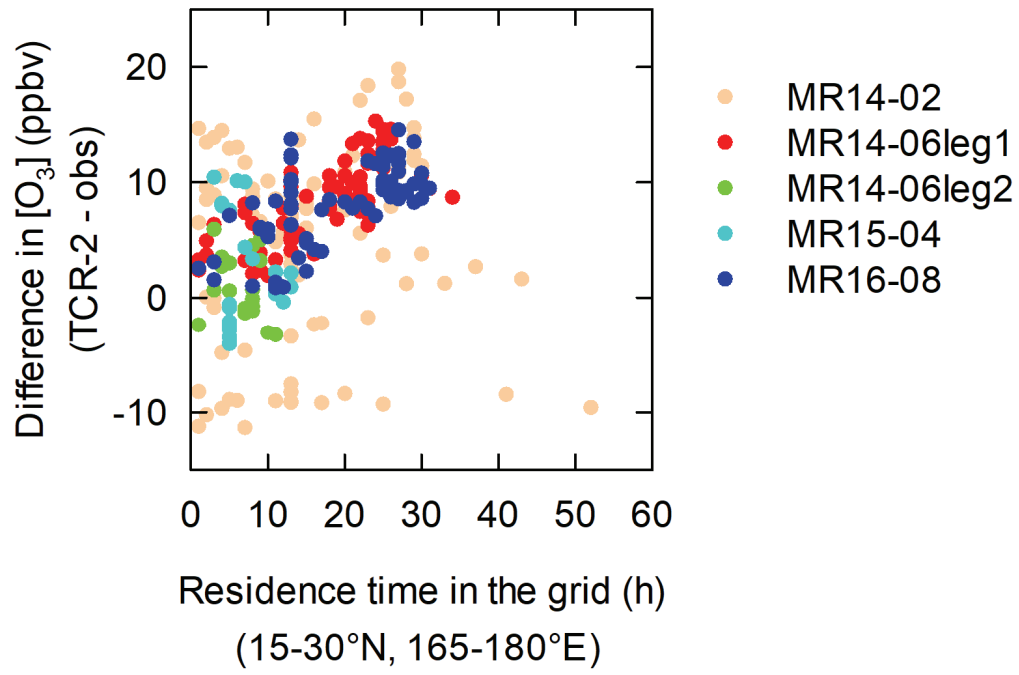
Figure 14. High biases in TCR-2 with respect to observations in domain 3 (0–15° N and 150–165° E) show positive correlations with daytime residence times in grid 15–30° N and 165–180° E.